Monthly Notices of the ROYAL ASTRONOMICAL SOCIETY

MNRAS **464,** 2403–2418 (2017) doi:10.1093/mnras/stw2454
Advance Access publication 2016 September 27

Probing the magnetic fields in L1415 and L1389

A. Soam,[1,2★] Chang Won Lee,[1,3] G. Maheswar,[2] Gwanjeong Kim,[1,3] S. Neha[2,4] and Mi-Ryang Kim[1,5]

[1]*Korea Astronomy and Space Science Institute (KASI), 776 Daedeokdae-ro, Yuseong-gu, Daejeon 305-348, Republic of Korea*
[2]*Aryabhatta Research Institute of Observational Sciences (ARIES), Nainital 263002, India*
[3]*University of Science and Technology, 176 Gajeong-dong, Yuseong-gu, Daejeon 305-350, Republic of Korea*
[4]*Pt. Ravishankar Shukla University, Amanaka G.E. Road, Raipur, Chhatisgarh 492010, India*
[5]*Chungbuk National University, Chungdae-ro 1, Seowon-gu, Cheongju, Chungbuk 28644, Republic of Korea*

Accepted 2016 September 26. Received 2016 September 23; in original form 2016 July 6; Editorial Decision 2016 September 23

ABSTRACT

We present the *R*-band polarimetric results towards two nebulae L1415 and L1389 containing low-luminosity stars. Aim of this study is to understand the role played by magnetic fields in formation of low-luminosity objects. Linear polarization arises due to dichroism of the background starlight projected on the cloud providing the plane-of-the sky magnetic field orientation. The offsets between mean magnetic field directions obtained towards L1415 and L1389 and the projected outflow axes are found to be 35° and 12°, respectively. The offset between cloud minor axes and mean envelope magnetic field direction in L1415 and L1389 are 50° and 87°, respectively. To estimate the magnetic field strength by using the updated Chandrasekhar–Fermi (CF) relation, we obtained the ^{12}CO(J = 1−0) line velocity dispersion value towards L1415 cloud using the Taeduk Radio Astronomical Observatory single dish observations. The values of $B_{\rm pos}$ in L1415 and L1389 are found to be 28 and 149 μG using CF technique and 23 and 140 μG using structure function analysis, respectively. The values of $B_{\rm pos}$ in these clouds are found to be consistent using both the techniques. By combining the present results with those obtained from our previous study of magnetic fields in cores with Very Low Luminosity Objects (VeLLOs), we attempt to improve the sample of cores with low-luminosity protostars and bridge the gap between the understanding of importance of magnetic fields in cores with VeLLOs and low-luminosity protostars. The results of this work and that of our previous work show that the outflow directions are aligned with envelope magnetic fields of the clouds.

Key words: ISM: clouds – ISM: magnetic fields.

1 INTRODUCTION

In spite of the major progress in understanding the process of low-mass star formation in the past three decades (e.g. volumes by Levy & Lunine 1993), the earliest stages of the low-mass star formation remains poorly known. According to the present idea of low-mass star formation (Shu, Adams & Lizano 1987) in isolated cores, the gravitationally bound dense starless cores are the first evolutionary phase in the path of molecular clouds to the formation of stars. It is believed that the key ingredients involved in the star formation are gravity, magnetic fields and turbulence. The influence of magnetic field on various stages of star formation is not clearly known. In the magnetic field dominated scenario, the prestellar cores (cores on the verge of star formation; Ward-Thompson et al. 1994) are thought to be initially supported against their self-gravity by magnetic fields and evolve to higher central condensation through Ambipolar-diffusion (Mouschovias 1991). In the magnetically dominated scenario, the material is settled in a disc-like structure. This disc-like structure is of few thousands astronomical unit in size. This mediation of material by the field lines can later result into the magnetic fields parallel to the symmetry axis of the disc-like structure. A pinched hour glass morphology of field lines is seen in the inner core region within the infall radius (Fiedler & Mouschovias 1993; Galli & Shu 1993). The field lines in the envelope can be moderately pinched and join smoothly with the inner field lines. But in the cores where magnetic field play relatively lesser role, the available studies (Mac Low & Klessen 2004; Dib et al. 2007, 2010) suggest that the clumps and subsequent cores are formed on the junctions of the turbulent flows with supersonic motions. The supersonic turbulent flows can randomize the weaker magnetic field geometry (Crutcher 2004). Now these models can/should be tested

★ E-mail: archana@kasi.re.kr

by mapping the magnetic fields on the different spatial scales of the clouds and cores. Such studies can help in finding the correlations (if present) in the various cloud properties such as minor axes, bipolar outflows and kinematics with the magnetic field morphology.

The plane-of-the-sky magnetic field maps of dense cores are produced using polarization measurements in near-infrared and optical wavelengths caused due to the selective extinction of background starlight (Dennison 1977; Lazarian 2003). The preferential extinction of the background starlight is caused by the presence of elongated dust grains which are aligned with their minor axes parallel to the ambient magnetic fields. The actual mechanism by which these dust grains align with the magnetic fields is still under debate (Lazarian 2007; Andersson, Lazarian & Vaillancourt 2015). However, radiative torque mechanism, first proposed by Dolginov & Mitrofanov (1976), seems to be emerging as the most successful one in explaining the dust grain alignment in various environments (e.g. Hoang & Lazarian 2014; Andersson et al. 2015; Hoang, Lazarian & Andersson 2015).

We have chosen a poorly studied cloud L1415 for our present work. This cloud is classified as opacity class 3 and consist of a low-luminosity protostar ($0.13\,L_{\odot}$) namely IRAS 04376+5413 (Stecklum, Melnikov & Meusinger 2007). In this study, we are showing the *R*-band polarization results towards L1415 region with an aim to map and study the plane-of-the-sky magnetic field morphology in the low-density regions of this cloud. We made ^{12}CO(J = 1−0) molecular line observations of this cloud to estimate the velocity dispersion in the cloud which is required to estimate the magnetic field strength.

For our study, we also selected another cloud L1389, a cometary-shaped cloud (Launhardt et al. 2013) with a round head (consisting of *IRAS* source) and sharp tail. This cloud is located nearby Perseus and is associated with the Lindbald ring (Lindblad et al. 1973). *Herschel*-SPIRE images of L1389 clearly show a cometary morphology of the cloud (Launhardt et al. 2013). Based on the results of available infrared (IR) and (sub)millimetre continuum observations, Launhardt et al. (2010) found two sources present in L1389 cloud head. One source is found as L1389-IRS and dominates the IR emission in the *Spitzer* images but it has a faint millimetre continuum emission. But the other source is referred as L1389-SMM and it has no IR emission in *Spitzer*. On the contrary, this source is found to be with millimetre continuum emission. The spectral energy distributions fitting results from Chen et al. (2012) indicated that L1389-IRS may be a Class 0/I transition object while L1389-SMM (also referred as L1389-MMS) may be a pre-stellar core but later when they compared this source with pre-stellar cores and Class 0 protostars and found that L1389-MMS is more evolved than pre-stellar cores but less evolved than Class 0 protostars. They also found that the observed characteristics of this source are similar to the theoretical predictions from radiative/magnetohydrodynamical simulations of first hydrostatic core (Larson 1969; Masunaga, Miyama & Inutsuka 1998). But they also suggested that this source may be a possible extremely low luminosity star embedded in an edge-on disc. L1389-IRS is directly observed in the near-IR wavelengths (Launhardt et al. 2010), which means it can be a Class 0/I transition object with a luminosity of $L_{\mathrm{bol}} \sim 0.5\,L_{\odot}$. The estimated luminosity of L1389-MMS is found to be less than $0.04\,L_{\odot}$ (Chen et al. 2012).

This paper is organized such that Section 2 describes the methods of data acquisition and reduction procedure using optical polarimetric technique and ^{12}CO(1−0) molecular line observations. In Section 3, we present our results of optical polarization and molecular line observations. In Section 4, we discuss the procedure used to subtract the foreground polarization contribution. We also discuss the magnetic field geometry and strength in the same section. Finally, we conclude our paper by summarizing the results in Section 5.

Table 1. Log of optical polarization and radio observations.

Cloud	Polarization observation Observation date (year, month, date)	Band
L1415	2011 November 23 and 26; 2011 December 19, 20 and 24 2013 October 29	R_c
L1389	2011 November 26; 2013 October 28, 29	R_c
	Radio observation	
Cloud	Observation date (year, month, date)	Freq.
L1415	2016 March 4	115 GHz

2 OBSERVATIONS AND DATA REDUCTION

2.1 Optical polarization

The log of the *R*-band polarimetric observations of eight fields towards L1415 and four fields towards L1389 is shown in Table 1. We made these observation from Aries IMaging POLarimeter i.e. AIMPOL (Rautela, Joshi & Pandey 2004). This polarimeter is a back-end instrument on 1-m diameter optical telescope at Aryabhatta Research Institute of Observational Sciences, India. AIMPOL consists of an achromatic half-wave plate (HWP) modulator and a Wollaston prism beam-splitter. The images were obtained with the use of 1024 × 1024 pixel^2 CCD chip (Tektronix; TK1024) out of which central 325 × 325 pixel^2 area is used for the imaging because of the ∼8 arcmin diameter field of view of the CCD with plate scale 1.48 arcsec pixel^{-1}. The stellar image size falls in 2 to 3 pixels. The gain and read out noise of CCD are 11.98 e^- and 7.0 e^- per ADU, respectively.

The imaging polarimeters use a polarization modulator followed by an analyser to convert any polarized component into a light intensity. Fluxes of ordinary (I_o) and extraordinary (I_e) beams for all the observed sources with a good signal-to-noise ratio were extracted by standard aperture photometry using the IRAF package. The ratio $R(\alpha)$ is obtained as

$$R(\alpha) = \frac{\frac{I_e(\alpha)}{I_o(\alpha)} - 1}{\frac{I_e(\alpha)}{I_o(\alpha)} + 1} = P\cos(2\theta - 4\alpha), \tag{1}$$

where P is the degree of polarization and θ is the position angle of the plane of polarization. Here, α is the orientation of the fast axis of HWP at 0°, 22°.5, 45° and 67°.5 corresponding to four normalized Stokes parameters, respectively, $q[R(0^\circ)]$, $u[R(22.5^\circ)]$, $q_1[R(45^\circ)]$ and $u_1[R(67.5^\circ)]$. We estimated the errors in normalized Stokes parameters $(\sigma_R)(\alpha)(\sigma_q, \sigma_u, \sigma_{q1}, \sigma_{u1})$ using the relation provided by Ramaprakash et al. (1998).

The instrumental polarization of AIMPOL has been checked by observing unpolarized standards and found nearly invariable with a value of ∼0.1 per cent by Soam et al. (2013, 2015) and Neha et al. (2016). The polarized standard stars observed by us to calibrate our polarization values are summarized in Table 2.

2.2 Radio observations

We carried out the On-The-Fly (OTF) mapping observations of a region of 25 arcmin × 25 arcmin around L1415-IRS in ^{12}CO(1−0) and C^{18}O(1−0) molecular line simultaneously on 2016 March 04

Table 2. Polarized standard stars observed in R_c band.

Date of Obs.	P ± ϵ_P %	$\theta \pm \epsilon_\theta$ (°)
HD 236633 ([a]Standard values: 5.38 ± 0.02 per cent, 93°.04 ± 0°.15)		
2011 November 26	5.3 ± 0.1	92 ± 1
2011 December 19	5.5 ± 0.1	93 ± 1
2011 December 20	5.3 ± 0.2	93 ± 2
2011 December 24	5.7 ± 0.2	93 ± 1
HD 236954 ([b]Standard values: 5.79 ± 0.09 per cent, 111°.20 ± 0°.49)		
2011 December 2011	6.0 ± 0.1	111 ± 2
BD+59°389 ([a]Standard values: 6.43 ± 0.02 per cent, 98°.14 ± 0°.10)		
2011 November 26	7.0 ± 0.2	98 ± 1
2011 December 19	7.7 ± 0.2	99 ± 1
2011 December 20	6.2 ± 0.1	98 ± 1
2011 December 24	6.4 ± 0.1	98 ± 1
HD 204827 ([a]Standard values: 4.89 ± 0.03 per cent, 59°.10 ± 0°.17)		
2013 October 20	5.0 ± 0.2	66 ± 7
HD 19820 ([a]Standard values: 4.53 ± 0.02 per cent, 114°.46 ± 0°.16)		
2013 October 20	4.5 ± 0.1	116 ± 1

Notes. [a]Values in *R* band from Schmidt, Elston & Lupie (1992).
[b]Values in *V* band from Schmidt et al. (1992).

using the instrument SEcond QUabbin Observatory Imaging Array (SEQUOIA) at Taeduk Radio Astronomical Observatory (TRAO). TRAO is a millimetre-wave radio observation facility with a single dish of 13.7-m diameter at Korea Astronomy and Space Science Institute (KASI) in Daejeon, South Korea. SEQUOIA-TRAO is equipped with high-performing 16 pixel MMIC preamplifiers in a 4×4 array, operating within 85∼115 GHz frequency range. The system temperature is ranging from 250 K (86 ∼ 110 GHz) to 500 K (115 GHz; ^{12}CO). As the optical system provides two sideband, two different lines can be observed simultaneously. The sky signals were subtracted in position switch mode. The beam size Half Power Beam Width (HPBW) and main beam efficiency of the telescope are about 44 arcsec and 54 ± 2 per cent at 115 GHz, respectively (TRAO staff private communication). The integration time of OTF mapping was ∼180 min to achieve an rms of 0.3 K in $T_A{}^*$ scale in both the line. The signal-to-noise ratio is measured to be ∼16 at a brightest position of $T_A{}^* \sim 4.8$ K. The achieved velocity resolution is ∼0.2 km s^{-1}. The pointing and focus of the telescope was done using the source Orion A in SiO line. The pointing of the telescope was as good as ∼5–7 arcsec and the system temperature was within 500–650 K during the observations. The data were reduced by the CLASS software of the GILDAS package and further analysis was done using Common Astronomy Software Applications (CASA) and PYTHON language.

3 RESULTS

Results of our optical polarization measurements of stars projected on L1415 and L1389 are given in Table 3. The columns of the table give star number, corresponding right ascension (J2000) and the declination (J2000), the degree of polarization (P) in percent (per cent) and polarization angle ($\theta_{\rm P}$) in degree, respectively. The values of $\theta_{\rm P}$ are measured from north increasing towards east. The data points with ratio of P and the error in P ($\sigma_{\rm P}$), $\frac{P}{\sigma_{\rm P}} > 2$ are considered in this study.

Table 3. Polarization results of 224 stars observed in the direction of L1415 and 120 stars observed towards L1389.

Star Id	α (J2000) (°)	δ (J2000) (°)	P ± ϵ_P (%)	$\theta \pm \epsilon_\theta$ (°)
		L1415		
1	70.1670	54.2233	3.3 ± 0.6	168 ± 5
2	70.1901	54.2042	3.4 ± 0.3	158 ± 2
3	70.2008	54.1868	2.0 ± 0.3	154 ± 5
4	70.2025	54.2439	3.3 ± 0.2	152 ± 2
5	70.2117	54.1901	2.8 ± 0.1	152 ± 0
6	70.2238	54.3479	4.0 ± 0.6	159 ± 4
7	70.2299	54.1878	2.1 ± 0.6	146 ± 8
8	70.2351	54.3925	6.0 ± 1.0	141 ± 5
9	70.2356	54.2056	3.6 ± 0.2	150 ± 1
10	70.2364	54.2121	3.9 ± 0.1	151 ± 0
11	70.2376	54.2705	4.6 ± 0.2	152 ± 1
12	70.2378	54.3296	3.8 ± 0.4	139 ± 3
13	70.2383	54.2538	4.3 ± 0.7	154 ± 4
14	70.2423	54.2291	3.3 ± 0.1	153 ± 1
15	70.2427	54.3624	3.5 ± 1.3	155 ± 10
16	70.2509	54.3584	2.1 ± 0.4	179 ± 5
17	70.2519	54.3844	4.2 ± 0.6	154 ± 4
18	70.2528	54.2609	4.0 ± 0.1	150 ± 0
19	70.2538	54.1760	3.7 ± 0.8	160 ± 6
20	70.2563	54.2748	2.0 ± 0.4	142 ± 6
21	70.2580	54.3528	3.6 ± 0.4	151 ± 3
22	70.2590	54.2333	3.6 ± 0.1	153 ± 1
23	70.2645	54.1940	3.2 ± 0.1	149 ± 1
24	70.2684	54.2118	3.2 ± 0.4	146 ± 3
25	70.2719	54.2730	2.7 ± 0.4	143 ± 4
26	70.2722	54.3548	3.5 ± 0.6	153 ± 5
27	70.2731	54.3245	3.5 ± 0.6	168 ± 4
28	70.2768	54.3127	3.5 ± 0.8	161 ± 6
29	70.2786	54.2239	2.9 ± 0.2	150 ± 1
30	70.2798	54.3449	5.2 ± 1.1	155 ± 6
31	70.2800	54.2042	2.8 ± 0.3	148 ± 3
32	70.2803	54.3630	6.0 ± 0.9	154 ± 4
33	70.2809	54.2140	2.5 ± 0.8	147 ± 9
34	70.2826	54.1959	4.2 ± 0.6	160 ± 4
35	70.2836	54.2461	2.5 ± 0.1	154 ± 2
36	70.2843	54.1933	4.3 ± 0.6	151 ± 4
37	70.2847	54.3894	5.6 ± 0.3	152 ± 1
38	70.2874	54.3880	4.4 ± 1.2	163 ± 7
39	70.2894	54.2192	3.4 ± 0.6	147 ± 5
40	70.2910	54.4162	4.0 ± 0.2	163 ± 1
41	70.2923	54.2490	3.8 ± 0.5	154 ± 3
42	70.2952	54.2522	4.0 ± 0.2	150 ± 1
43	70.2953	54.2484	2.7 ± 0.7	149 ± 7
44	70.3018	54.2512	2.7 ± 0.7	145 ± 7
45	70.3043	54.5014	3.0 ± 0.6	166 ± 6
46	70.3050	54.4148	4.4 ± 0.1	159 ± 0
47	70.3084	54.3108	3.7 ± 0.5	148 ± 4
48	70.3118	54.2689	4.0 ± 0.4	147 ± 2
49	70.3123	54.2023	4.2 ± 1.4	152 ± 9
50	70.3136	54.4179	5.3 ± 1.8	171 ± 9
51	70.3158	54.4139	4.5 ± 0.9	160 ± 5
52	70.3165	54.1809	3.0 ± 0.3	152 ± 3
53	70.3203	54.4078	1.0 ± 0.2	151 ± 7
54	70.3219	54.1934	3.7 ± 0.6	153 ± 4
55	70.3277	54.4188	4.5 ± 0.6	165 ± 4
56	70.3291	54.3568	3.7 ± 0.3	155 ± 2

Table 3 – *continued*

Star Id	α (J2000) (°)	δ (J2000) (°)	P ± ϵ_P (%)	θ ± ϵ_θ (°)
57	70.3343	54.2485	2.9 ± 0.9	143 ± 8
58	70.3409	54.1984	3.9 ± 0.3	155 ± 2
59	70.3457	54.2363	5.1 ± 0.5	157 ± 2
60	70.3507	54.3522	4.4 ± 0.4	154 ± 2
61	70.3590	54.5180	1.2 ± 0.5	172 ± 12
62	70.3590	54.3734	7.2 ± 0.7	156 ± 2
63	70.3619	54.2404	3.3 ± 0.4	152 ± 3
64	70.3621	54.5015	1.9 ± 0.3	167 ± 4
65	70.3723	54.2383	3.3 ± 0.3	155 ± 3
66	70.3762	54.3372	0.8 ± 0.3	162 ± 11
67	70.3776	54.5088	2.1 ± 0.3	173 ± 4
68	70.3819	54.4391	1.7 ± 0.5	170 ± 8
69	70.3877	54.5447	1.5 ± 0.4	149 ± 7
70	70.4012	54.5110	2.2 ± 0.3	152 ± 4
71	70.4490	54.2801	4.9 ± 0.9	174 ± 5
72	70.4525	54.4072	3.2 ± 0.3	144 ± 3
73	70.4546	54.5076	2.6 ± 0.1	154 ± 1
74	70.4650	54.2872	4.9 ± 0.1	164 ± 1
75	70.4653	54.2880	5.7 ± 2.4	161 ± 12
76	70.4699	54.4338	1.6 ± 0.7	146 ± 11
77	70.4783	54.4571	1.3 ± 0.3	172 ± 7
78	70.4814	54.2858	5.1 ± 0.6	157 ± 3
79	70.4819	54.2186	4.0 ± 0.3	153 ± 2
80	70.4839	54.2579	5.7 ± 1.2	155 ± 6
81	70.4861	54.4030	2.7 ± 0.9	139 ± 9
82	70.4861	54.4030	2.7 ± 0.9	139 ± 9
83	70.4867	54.4050	2.1 ± 0.1	139 ± 1
84	70.4916	54.2647	3.6 ± 1.6	167 ± 12
85	70.4930	54.2799	4.6 ± 0.7	156 ± 4
86	70.4941	54.4454	1.9 ± 0.8	171 ± 12
87	70.4951	54.4455	1.9 ± 0.4	174 ± 5
88	70.4956	54.4306	1.0 ± 0.3	175 ± 8
89	70.4964	54.2582	1.3 ± 0.2	172 ± 4
90	70.4974	54.4034	2.5 ± 0.7	144 ± 8
91	70.4984	54.2376	5.8 ± 0.9	150 ± 4
92	70.5006	54.2579	4.3 ± 0.8	149 ± 5
93	70.5096	54.4286	2.9 ± 0.1	167 ± 1
94	70.5151	54.2370	4.3 ± 1.3	152 ± 8
95	70.5215	54.4471	0.8 ± 0.2	179 ± 8
96	70.5244	54.2413	1.0 ± 0.3	175 ± 7
97	70.5251	54.3035	2.4 ± 0.6	145 ± 7
98	70.5265	54.3793	5.0 ± 0.6	148 ± 3
99	70.5282	54.2902	3.0 ± 0.4	158 ± 4
100	70.5287	54.4221	3.5 ± 0.6	156 ± 5
101	70.5289	54.4220	1.9 ± 0.8	174 ± 11
102	70.5307	54.4046	1.9 ± 0.4	154 ± 6
103	70.5309	54.4046	2.2 ± 0.6	153 ± 7
104	70.5322	54.4055	1.8 ± 0.4	158 ± 6
105	70.5362	54.3861	5.4 ± 0.5	176 ± 3
106	70.5363	54.3860	4.1 ± 0.8	152 ± 5
107	70.5374	54.4618	2.4 ± 1.1	165 ± 12
108	70.5403	54.2557	1.8 ± 0.3	155 ± 5
109	70.5506	54.4335	3.2 ± 0.7	153 ± 6
110	70.5508	54.4335	2.5 ± 0.7	172 ± 7
111	70.5513	54.3673	4.4 ± 0.4	155 ± 3
112	70.5513	54.3673	4.4 ± 0.4	155 ± 3
113	70.5518	54.2333	3.4 ± 0.2	151 ± 2
114	70.5520	54.4388	3.6 ± 0.9	145 ± 7
115	70.5525	54.4832	1.9 ± 0.1	161 ± 1

Table 3 – *continued*

Star Id	α (J2000) (°)	δ (J2000) (°)	P ± ϵ_P (%)	θ ± ϵ_θ (°)
116	70.5543	54.2064	7.4 ± 0.8	144 ± 3
117	70.5553	54.2148	2.4 ± 0.3	133 ± 3
118	70.5557	54.3012	2.4 ± 0.8	161 ± 9
119	70.5560	54.2295	3.9 ± 0.9	147 ± 6
120	70.5564	54.2446	4.3 ± 1.1	157 ± 7
121	70.5596	54.4184	3.0 ± 0.2	166 ± 2
122	70.5598	54.4183	3.0 ± 0.2	170 ± 2
123	70.5599	54.4183	3.3 ± 0.2	171 ± 1
124	70.5601	54.2201	2.1 ± 0.4	135 ± 5
125	70.5613	54.2546	3.0 ± 0.9	161 ± 8
126	70.5685	54.2146	1.6 ± 0.1	147 ± 1
127	70.5706	54.4824	1.1 ± 0.2	167 ± 5
128	70.5746	54.2202	1.3 ± 0.3	133 ± 7
129	70.5768	54.4388	1.6 ± 0.3	175 ± 6
130	70.5768	54.4389	1.1 ± 0.2	179 ± 6
131	70.5768	54.4129	5.2 ± 0.9	166 ± 4
132	70.5775	54.2526	2.1 ± 1.0	161 ± 12
133	70.5804	54.2515	2.9 ± 0.4	159 ± 4
134	70.5870	54.2569	2.9 ± 1.3	145 ± 12
135	70.5878	54.4501	0.7 ± 0.2	174 ± 8
136	70.5890	54.4078	3.2 ± 0.5	158 ± 5
137	70.5891	54.4077	3.0 ± 0.8	171 ± 7
138	70.5891	54.4077	2.9 ± 0.6	171 ± 5
139	70.5892	54.2546	3.1 ± 0.4	152 ± 4
140	70.5895	54.4752	1.5 ± 0.7	173 ± 12
141	70.5898	54.4727	3.2 ± 0.6	172 ± 5
142	70.5924	54.2316	2.1 ± 0.5	126 ± 6
143	70.5944	54.4206	3.2 ± 0.6	164 ± 6
144	70.5945	54.4205	3.3 ± 0.6	174 ± 5
145	70.5946	54.4206	3.3 ± 0.5	169 ± 4
146	70.5961	54.3854	2.2 ± 0.3	160 ± 4
147	70.5961	54.3854	2.1 ± 0.2	157 ± 3
148	70.5968	54.2469	1.2 ± 0.2	158 ± 5
149	70.5978	54.4714	1.0 ± 0.3	179 ± 8
150	70.5984	54.4010	3.1 ± 0.8	166 ± 6
151	70.5985	54.4010	2.9 ± 1.0	145 ± 9
152	70.5985	54.4011	4.0 ± 1.0	169 ± 8
153	70.5991	54.2382	2.8 ± 0.5	142 ± 5
154	70.5999	54.2878	4.7 ± 0.9	156 ± 5
155	70.6018	54.4323	3.4 ± 0.4	158 ± 3
156	70.6019	54.4322	3.1 ± 0.3	162 ± 3
157	70.6046	54.4876	0.8 ± 0.1	155 ± 5
158	70.6050	54.4142	2.5 ± 0.1	153 ± 2
159	70.6050	54.4142	2.3 ± 0.1	160 ± 1
160	70.6050	54.4142	1.9 ± 0.1	164 ± 2
161	70.6111	54.3892	1.6 ± 0.3	150 ± 5
162	70.6111	54.3892	1.7 ± 0.3	148 ± 5
163	70.6111	54.3892	1.5 ± 0.3	153 ± 6
164	70.6114	54.2784	1.9 ± 0.5	150 ± 7
165	70.6149	54.2324	1.6 ± 0.3	148 ± 5
166	70.6173	54.4155	3.0 ± 0.4	151 ± 3
167	70.6174	54.4155	2.6 ± 0.6	154 ± 6
168	70.6209	54.3918	3.1 ± 0.5	165 ± 4
169	70.6209	54.3919	2.3 ± 0.6	161 ± 8
170	70.6212	54.4939	1.1 ± 0.4	156 ± 9
171	70.6258	54.4067	4.6 ± 1.5	152 ± 9
172	70.6284	54.3806	2.3 ± 0.7	133 ± 8

Table 3 – *continued*

Star Id	α (J2000) (°)	δ (J2000) (°)	P $\pm \epsilon_P$ (%)	$\theta \pm \epsilon_\theta$ (°)
173	70.6334	54.4058	2.5 ± 1.0	162 ± 10
174	70.6340	54.4247	3.4 ± 1.1	146 ± 9
175	70.6376	54.4888	1.2 ± 0.3	167 ± 7
176	70.6390	54.2297	1.5 ± 0.6	124 ± 10
177	70.6400	54.4911	1.6 ± 0.4	163 ± 6
178	70.6406	54.3840	3.2 ± 0.4	135 ± 3
179	70.6406	54.3840	3.1 ± 0.4	127 ± 3
180	70.6506	54.5006	2.2 ± 0.8	157 ± 10
181	70.6571	54.4084	4.1 ± 1.1	160 ± 7
182	70.6684	54.4058	4.5 ± 1.1	153 ± 7
183	70.6684	54.4058	5.9 ± 1.1	133 ± 4
184	70.6726	54.4609	1.6 ± 0.1	157 ± 1
185	70.6765	54.4570	1.3 ± 0.4	166 ± 8
186	70.6772	54.4604	2.3 ± 0.4	155 ± 4
187	70.6780	54.4636	2.1 ± 0.3	169 ± 4
188	70.6794	54.3912	3.9 ± 0.7	152 ± 5
189	70.6806	54.3941	2.7 ± 0.3	135 ± 2
190	70.6828	54.4090	1.2 ± 0.1	176 ± 2
191	70.6828	54.4089	0.9 ± 0.1	159 ± 3
192	70.6844	54.2896	4.4 ± 0.1	157 ± 0
193	70.6898	54.4716	4.0 ± 0.8	147 ± 6
194	70.6899	54.4804	1.0 ± 0.5	145 ± 13
195	70.6916	54.4223	1.4 ± 0.7	160 ± 12
196	70.6977	54.4736	1.6 ± 0.3	147 ± 6
197	70.6989	54.3668	0.7 ± 0.2	158 ± 7
198	70.7005	54.4393	2.3 ± 0.5	149 ± 6
199	70.7014	54.3353	2.6 ± 0.2	169 ± 2
200	70.7026	54.4625	3.2 ± 1.2	160 ± 10
201	70.7060	54.3204	2.6 ± 0.1	157 ± 1
202	70.7141	54.2462	2.9 ± 0.7	149 ± 6
203	70.7263	54.3366	0.7 ± 0.1	165 ± 4
204	70.7283	54.2612	3.8 ± 1.4	153 ± 10
205	70.7288	54.4292	2.6 ± 1.1	169 ± 11
206	70.7340	54.3414	1.8 ± 0.8	149 ± 13
207	70.7367	54.3438	2.3 ± 0.7	133 ± 8
208	70.7394	54.2847	4.5 ± 0.2	153 ± 1
209	70.7395	54.4522	0.8 ± 0.1	166 ± 2
210	70.7428	54.2850	4.7 ± 0.3	150 ± 1
211	70.7515	54.2677	4.5 ± 1.2	140 ± 7
212	70.7527	54.2716	5.1 ± 1.1	150 ± 6
213	70.7606	54.2624	0.8 ± 0.2	174 ± 6
214	70.7610	54.3067	3.3 ± 1.6	156 ± 13
215	70.7747	54.2369	2.7 ± 0.5	149 ± 5
216	70.7762	54.2649	4.3 ± 0.4	147 ± 3
217	70.7783	54.3027	4.0 ± 0.9	153 ± 6
218	70.7816	54.2471	2.7 ± 0.3	144 ± 3
219	70.7924	54.2499	3.4 ± 0.3	142 ± 3
220	70.8041	54.2840	3.4 ± 0.4	153 ± 3
221	70.8043	54.2788	3.2 ± 0.5	148 ± 4
222	70.8062	54.2762	3.0 ± 1.0	156 ± 9
223	70.8280	54.2748	3.9 ± 0.8	143 ± 5
224	70.8511	54.2709	1.6 ± 0.5	125 ± 8
		L1389		
1	61.0506	56.9603	4.0 ± 0.7	134 ± 5
2	61.0506	56.9603	4.0 ± 0.7	134 ± 5
3	61.0508	56.9344	4.6 ± 0.3	136 ± 2
4	61.0621	56.9307	1.3 ± 0.3	118 ± 6
5	61.0655	56.9464	1.0 ± 0.2	136 ± 7
6	61.0763	56.9219	3.8 ± 1.8	148 ± 13

Table 3 – *continued*

Star Id	α (J2000) (°)	δ (J2000) (°)	P $\pm \epsilon_P$ (%)	$\theta \pm \epsilon_\theta$ (°)
7	61.0820	56.9500	5.1 ± 1.4	138 ± 7
8	61.0865	56.9199	3.7 ± 0.9	128 ± 7
9	61.0898	56.9437	3.4 ± 0.5	137 ± 4
10	61.0935	57.1189	3.8 ± 0.4	121 ± 3
11	61.0946	56.9167	4.3 ± 1.1	142 ± 7
12	61.1010	56.9515	3.8 ± 0.4	137 ± 3
13	61.1061	56.9814	3.3 ± 1.2	137 ± 10
14	61.1101	57.1303	3.5 ± 0.5	129 ± 4
15	61.1129	56.9169	4.3 ± 0.6	140 ± 4
16	61.1149	56.9422	4.2 ± 0.2	139 ± 1
17	61.1161	56.9969	4.0 ± 1.0	133 ± 7
18	61.1201	56.9134	2.1 ± 0.1	136 ± 1
19	61.1232	56.9160	5.0 ± 1.2	143 ± 7
20	61.1313	57.1542	3.3 ± 0.1	136 ± 1
21	61.1314	56.9178	5.1 ± 0.6	129 ± 3
22	61.1390	57.1671	2.5 ± 0.3	135 ± 3
23	61.1391	56.9627	3.6 ± 0.3	134 ± 2
24	61.1394	57.1184	3.8 ± 0.4	139 ± 3
25	61.1397	56.9210	4.7 ± 1.8	127 ± 10
26	61.1431	56.8963	4.5 ± 1.4	144 ± 8
27	61.1434	56.8906	4.0 ± 1.8	137 ± 12
28	61.1455	57.1118	3.5 ± 0.1	134 ± 1
29	61.1471	57.1366	4.1 ± 0.3	134 ± 2
30	61.1480	57.0080	3.9 ± 0.5	140 ± 4
31	61.1493	56.9722	5.3 ± 0.4	139 ± 2
32	61.1517	57.0154	3.2 ± 0.6	142 ± 5
33	61.1521	57.0084	3.7 ± 0.6	136 ± 4
34	61.1526	57.1845	3.7 ± 0.1	137 ± 1
35	61.1543	57.0066	4.4 ± 0.4	138 ± 2
36	61.1584	56.9707	2.8 ± 0.8	144 ± 8
37	61.1639	56.8965	3.1 ± 0.8	145 ± 7
38	61.1640	57.1287	2.8 ± 0.8	135 ± 7
39	61.1659	57.1021	3.0 ± 0.5	129 ± 4
40	61.1677	57.1293	3.3 ± 0.5	136 ± 4
41	61.1766	56.9995	3.2 ± 0.3	157 ± 3
42	61.1807	57.1193	3.6 ± 0.5	132 ± 4
43	61.1816	57.1579	3.8 ± 0.2	133 ± 1
44	61.1864	57.0017	1.5 ± 0.4	133 ± 7
45	61.1876	57.0271	3.7 ± 0.5	137 ± 4
46	61.1976	57.1483	4.6 ± 0.6	131 ± 3
47	61.2021	56.9997	0.7 ± 0.1	129 ± 4
48	61.2063	57.0914	3.4 ± 0.1	132 ± 1
49	61.2119	57.0353	3.4 ± 0.6	144 ± 5
50	61.2125	57.0312	2.3 ± 0.5	138 ± 6
51	61.2127	57.0916	2.7 ± 0.1	135 ± 1
52	61.2129	57.0309	2.3 ± 0.2	138 ± 3
53	61.2137	57.0913	4.0 ± 0.3	133 ± 2
54	61.2154	56.9815	2.3 ± 0.2	135 ± 3
55	61.2156	56.9333	4.0 ± 1.6	139 ± 11
56	61.2176	57.1152	3.3 ± 0.5	135 ± 4
57	61.2186	57.1151	2.9 ± 0.4	132 ± 4
58	61.2202	57.1592	3.0 ± 0.6	132 ± 6
59	61.2228	57.1960	3.1 ± 0.4	140 ± 3
60	61.2234	57.0616	3.7 ± 0.1	134 ± 2
61	61.2237	56.9011	2.5 ± 1.1	126 ± 11
62	61.2239	57.0236	1.5 ± 0.5	130 ± 9
63	61.2249	57.1955	2.2 ± 0.3	135 ± 4

Table 3 – *continued*

Star Id	α (J2000) (°)	δ (J2000) (°)	$P \pm \epsilon_P$ (%)	$\theta \pm \epsilon_\theta$ (°)
64	61.2256	57.1185	3.9 ± 0.1	130 ± 1
65	61.2265	57.1183	4.1 ± 0.1	129 ± 1
66	61.2267	57.0693	3.4 ± 0.1	134 ± 1
67	61.2270	57.0689	3.7 ± 0.1	134 ± 1
68	61.2295	57.0467	4.7 ± 0.9	135 ± 5
69	61.2310	57.1506	4.6 ± 0.4	130 ± 2
70	61.2310	57.0006	3.3 ± 0.1	135 ± 1
71	61.2318	56.9568	3.2 ± 1.3	133 ± 11
72	61.2344	56.9201	2.8 ± 0.2	137 ± 2
73	61.2347	56.9982	3.8 ± 0.4	137 ± 3
74	61.2381	56.9792	3.2 ± 0.4	134 ± 3
75	61.2391	57.1492	2.6 ± 0.3	137 ± 3
76	61.2407	57.0363	3.2 ± 0.3	145 ± 3
77	61.2431	57.1453	2.7 ± 0.1	137 ± 1
78	61.2438	57.0269	4.1 ± 0.6	132 ± 4
79	61.2462	57.1802	3.8 ± 0.4	134 ± 3
80	61.2479	57.0891	2.4 ± 0.1	134 ± 1
81	61.2521	57.0302	3.5 ± 0.4	131 ± 3
82	61.2569	56.9554	3.1 ± 0.7	141 ± 6
83	61.2617	57.0785	3.1 ± 0.2	136 ± 2
84	61.2624	57.1660	4.1 ± 0.9	126 ± 6
85	61.2645	57.1067	4.3 ± 0.4	135 ± 2
86	61.2655	57.1065	4.1 ± 0.4	134 ± 2
87	61.2663	57.0791	3.7 ± 0.1	138 ± 1
88	61.2667	57.1496	5.0 ± 0.6	128 ± 3
89	61.2762	56.9743	3.1 ± 0.1	137 ± 1
90	61.2773	57.0502	3.1 ± 0.7	128 ± 7
91	61.2785	57.1301	3.2 ± 0.1	136 ± 3
92	61.2796	57.0699	3.0 ± 0.2	143 ± 2
93	61.2798	57.0334	3.8 ± 0.4	135 ± 3
94	61.2799	57.0695	3.3 ± 0.2	141 ± 2
95	61.2800	57.1327	3.0 ± 0.1	140 ± 1
96	61.2801	57.0331	2.6 ± 0.4	132 ± 5
97	61.2812	56.9871	3.1 ± 0.1	143 ± 1
98	61.2886	57.0916	2.8 ± 0.3	137 ± 3
99	61.2915	57.0906	2.5 ± 0.4	133 ± 4
100	61.2969	57.1221	1.8 ± 0.2	123 ± 3
101	61.2979	57.1219	1.9 ± 0.2	129 ± 2
102	61.3064	56.9901	2.7 ± 0.3	130 ± 4
103	61.3095	57.0807	2.3 ± 0.6	124 ± 7
104	61.3140	57.0398	2.6 ± 0.2	133 ± 2
105	61.3144	57.0394	2.0 ± 0.2	130 ± 3
106	61.3170	57.0380	3.7 ± 0.4	142 ± 2
107	61.3176	57.0317	3.1 ± 0.7	141 ± 6
108	61.3230	57.0879	2.1 ± 0.1	138 ± 1
109	61.3266	56.9906	2.3 ± 0.6	142 ± 7
110	61.3327	57.0512	3.1 ± 0.3	138 ± 2
111	61.3327	56.9901	2.2 ± 0.2	138 ± 3
112	61.3330	57.0508	3.3 ± 0.3	133 ± 2
113	61.3352	56.9933	4.3 ± 0.8	141 ± 5
114	61.3359	56.9721	3.5 ± 0.4	123 ± 3
115	61.3419	57.0655	2.5 ± 0.2	132 ± 2
116	61.3492	57.0346	3.8 ± 0.3	133 ± 2
117	61.3513	57.0036	2.4 ± 0.2	131 ± 2
118	61.3559	57.0818	3.5 ± 0.3	132 ± 2
119	61.3609	57.0704	2.3 ± 0.5	148 ± 7
120	61.3687	57.0909	1.4 ± 0.1	137 ± 2

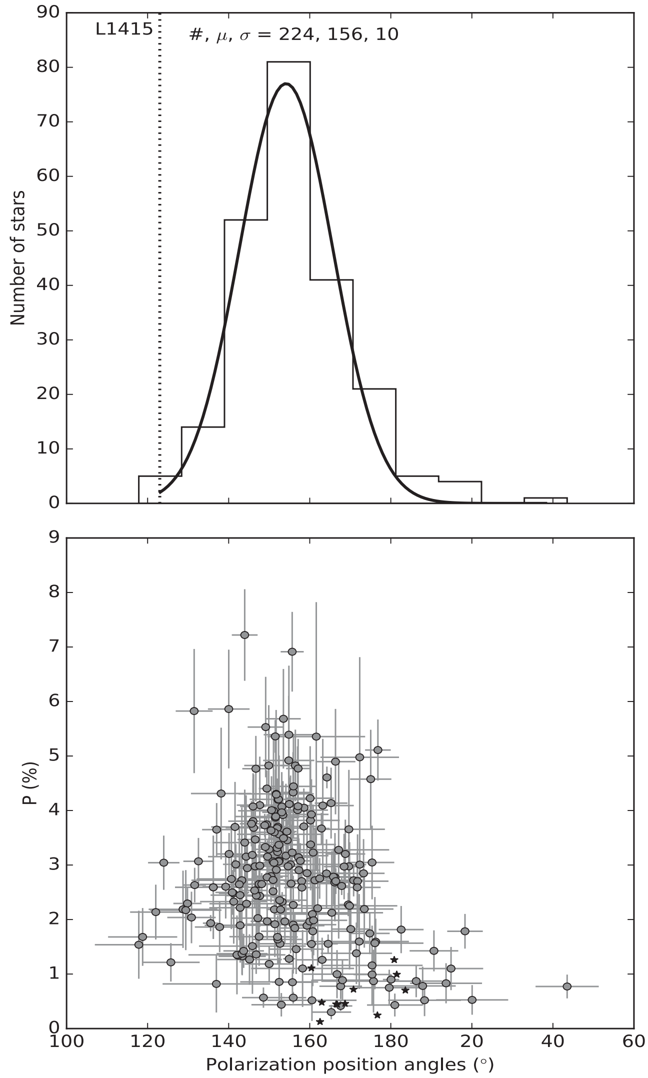

Figure 1. Upper panel: Gaussian-fitted histogram of θ_P with bin size 10° in L1415. The orientation of Galactic plane is drawn using dotted line. Lower panel: variation of P with θ_P of program stars and that of the stars which are foreground to the cloud L1415. Filled circles represent program stars and foreground stars are shown by filled star symbols.

Several reactions forming different molecules take place on the surface of the dust grains in the molecular clouds at their different evolutionary stages. These reaction can change the characteristics such as shape, size and composition of the grains. The grains located inside the denser parts of the molecular clouds are found to be bigger than the grains on the outer periphery (Wilking et al. 1980; Kandori et al. 2003; Whittet 2005; Olofsson & Olofsson 2010). The dust grains with the similar size as those on the outer regions of the clouds efficiently polarize the light in the optical wavelengths (Goodman 1996). Therefore, the magnetic field maps made in this study are in the lower density outer envelope regions of L1415 and L1389.

3.1 L1415

The polarization measurements for 224 stars observed towards dark nebula L1415 in R band are carried out in this work. The upper panel of Fig. 1 shows the Gaussian-fitted histogram of θ_P of the stars towards L1415. The lower panel of this figure shows the

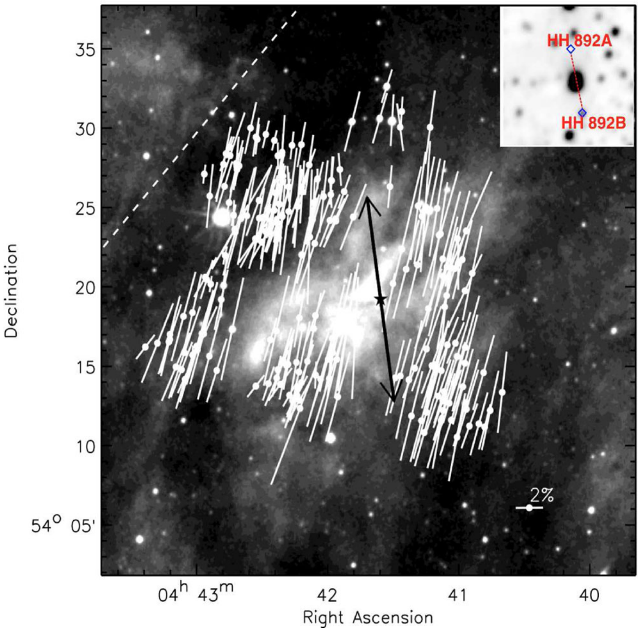

Figure 2. Overlaid polarization vectors of the stars projected on L1415 shown on 0.°6 × 0.°6 *WISE* 12 μm image after subtracting the foreground polarization contribution. The double arrow headed line shows the direction of CO outflow from L1415-IRS (shown by star symbol) and the dashed line shows the orientation of the Galactic plane. A vector with 2 per cent polarization is shown as reference. The inset shows the positions of HH objects (Stecklum et al. 2007) on 0.°04 × 0.°04 *WISE* 3.4 μm image of L1415.

P versus θ_P plot of these stars. In Fig. 2, we show the optical polarization vectors overlaid on 0.°6 × 0.°6 *WISE* 12 μm image of L1415. Here, the lengths of polarization vectors correspond to the degree of polarization. A vector with 2 per cent polarization is shown in the figure as a reference vector. The dashed-line shows the direction of Galactic plane with a plane of sky projection angle of 123°. The inset shows the positions of Herbig–Haro objects (HHOs; Stecklum et al. 2007) on 0.°04 × 0.°04 *WISE* 3.4 μm image of L1415. The mean values of *P* and θ_P with their corresponding standard deviation values are found to be 3.1 ± 1.3 per cent and 155±10°, respectively. Among the targets we observed, there are no peculiar-type stars and young stellar objects hence our polarization values can be used to estimate the local magnetic field properties of L1415. There are no near-IR and submillimetre polarization studies available towards L1415.

The evidence of well-collimated outflow is found to be associated with L1415-IRS, with the presence of HH 892 (Stecklum et al. 2007). The spectrum of HH 892A resembles to that of a high-excitation HHO (Raga & Canto 1996). An active Herbig–Haro flow towards L1415 has also been reported by Stecklum et al. (2007) based on the long-slit spectroscopic study. On the DSS image of L1415, an HHO candidate near IRAS 04376+5413 was detected (Stecklum et al. 2007). Using subsequent Hα and [S II] imaging, Stecklum et al. (2007) confirmed the presence of the emission line object with no counterpart. This HHO was assigned as 892 in Reipurth's catalogue (Reipurth 1999). The Near Infra Red (NIR) morphology of L1415-IRS also shows a bipolar nebulosity, with two lobes seen in 2.16 μm (Stecklum et al. 2007).

No prior studies have given any information of the major and minor axes of the cloud. We estimated the minor axis position angle of L1415 core by fitting an ellipse in *IRAS* 100 μm data (no *Herschel* and SCUBA[1] data are available for this cloud). We performed the photometry on the *IRAS* cores using the Cardiff Source-finding AlgoRithm (CSAR) based on CLUMPFIND. The CSAR is designed to find pre-stellar/starless clumps with the sizes in the range of ∼5000 au to 2.7 pc by removing background emission where the dense cores are embedded (Kirk et al. 2013). We calculated the background by averaging the pixel values outside the region over which the photometry is measured. Fig. 3 shows the ellipse fitted to the *IRAS* 100 μm image of L1415. CSAR works by sorting each pixel in the map with respect to signal-to-noise ratio in order of decreasing intensity. The ellipse is fitted at a level where the intensity value is basically the full width at half-maximum (FWHM) of the central pixel value and then falls gradually. The minor axis position angle of the fitted ellipse is found to be ∼25° which is the projection on the sky. We adopted this position angle for our further analysis of the results in L1415 cloud.

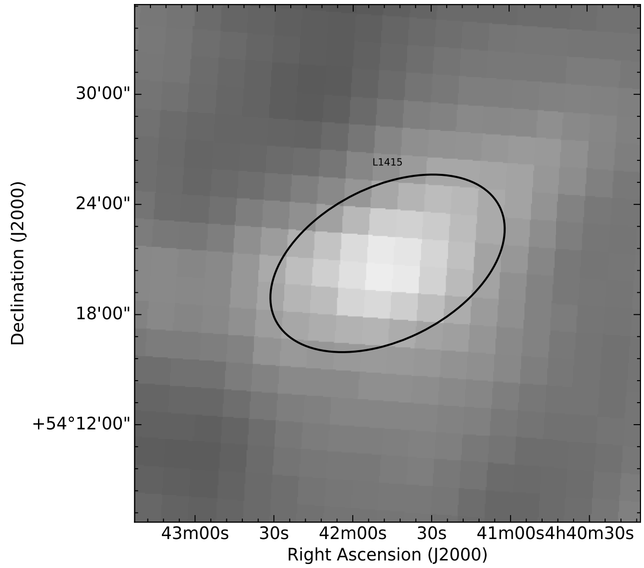

Figure 3. Ellipses fitted to the *IRAS* 100 μm image of L1415 for estimating the minor axis position angle using the CSAR based on CLUMPFIND.

3.2 Molecular line results in L1415

Fig. 4 shows *WISE* 12 μm image of L1415 with overplotted ^{12}CO(1−0) integrated intensity contours corresponding to two velocity components with V_{LSR} −5.5 km s^{-1} (white in left-hand panel) and −0.5 km s^{-1} (cyan in right-hand panel) found in the direction of L1415. The average spectra corresponding to the emissions are shown in the insets in both the panels. The images are also overlaid with optical polarization vectors in red colour. The positions of L1415-IRS and the outflow directions in both the panels are shown using black cross and the dashed line, respectively. The width of spectral line is generally expressed as FWHM and often the line profiles are well represented by Gaussian shape. From the OTF map in ^{12}CO(1−0) molecular line towards L1415, we estimated the ^{12}CO line width as it depicts the low-density region of the cloud where optical polarization observations are made. The average value of the ^{12}CO(1−0) line widths measured at various positions of the emission with V_{LSR} −5.5 km s^{-1} is found to be 1.65±0.02 km s^{-1}

[1] Submillimetre Common-User Bolometer Array on James Clark Maxwell Telescope.

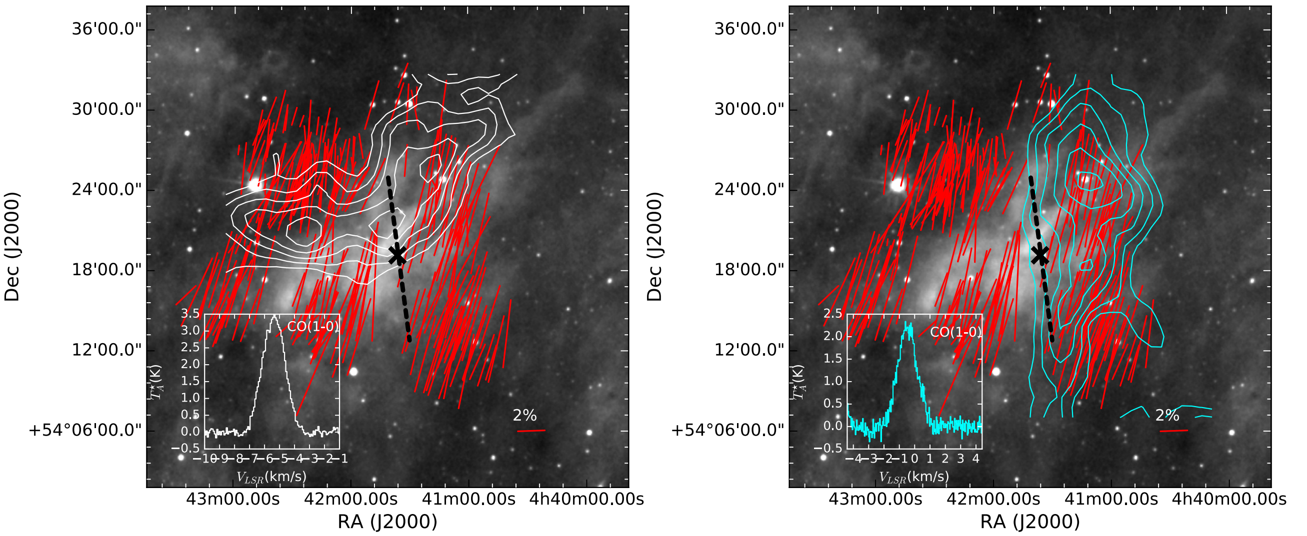

Figure 4. *WISE* 12 μm image of L1415 with overplotted ^{12}CO(1−0) integrated intensity contours corresponding to two velocity components with $V_{\rm LSR}$ −5.5 km s^{-1} (white in left-hand panel) and −0.5 km s^{-1} (cyan in right-hand panel) overlaid with optical polarization vectors in red colour. The contour levels for the integrated intensity in left-hand panel are drawn between 7.2 and 14.6 K km s^{-1} with an increment of 1.2 K km s^{-1}. The contour levels for the integrated intensity in right-hand panel are drawn between 63 and 188 K km s^{-1} with an increment of 9 K km s^{-1}. The average spectra corresponding to the emissions are shown in the insets in both the panels. The positions of L1415-IRS and the outflow directions in both the panels are shown using black cross and the dashed line, respectively.

and that of the other component with $V_{\rm LSR}$ −0.5 km s^{-1} is found to be 1.64±0.02 km s^{-1}. The width measurement in the spectra is done by fitting Gaussian to the lines using CLASS software.

We considered both the components of CO emissions important as they coincide with positions of the cloud where we made the optical polarimetric observations. We compared the polarization values of the stars corresponding to the two populations where two different velocity ^{12}CO components are dominant. The polarization results of these two populations are consistent. The mean values of the P corresponding to two samples are found to be 2.9 per cent and 3.4 per cent, respectively, and that of $\theta_{\rm P}$ are found to be 157° in each sample. The histograms of $\theta_{\rm P}$ and distribution of P with $\theta_{\rm P}$ corresponding to these two populations are shown in Fig. 5.

3.3 L1389

L1389 is a well-studied cloud but lacks the magnetic field information. We present the complete magnetic field morphology of L1389 by carrying out the polarization measurements of 120 stars projected on it. The Gaussian-fitted histogram of $\theta_{\rm P}$ measured in L1389 is shown in the upper panel of Fig. 6. The lower panel shows the variation of P with $\theta_{\rm P}$. The upper panel of Fig. 7 shows the optical polarization vectors overlaid on 0°.5 × 0°.5 *WISE* 12 μm image of L1389. A vector with 2 per cent polarization is shown in the figure as a reference vector. The dashed line shows the orientation of the Galactic plane with a plane-of-the-sky projection angle of 115°. The mean values of P and $\theta_{\rm P}$ with corresponding standard deviations are found to be 3.3±0.9 per cent and 137±6°, respectively.

L1389 has submillimetre polarization measurements available from SCUBA polarimeter (SCUBAPOL) in the catalogue made by Matthews et al. (2009). Although the sample is poor (only two polarization detection are available) with $P/\sigma_{\rm P} \geq 2$. We have adopted these measurements to assume a mean magnetic field morphology in the high-density region of L1389 core. The average values of the P and that of $\theta_{\rm P}$ with their corresponding standard deviation are found to be 19±5 per cent and 151±10°, respectively. The elongated dust grains aligned with magnetic fields make the thermal continuum emission polarized along their longer axes. Hence to infer the magnetic field geometry information, the submillimetre polarization vectors have to be rotated by 90° (Goodman 1996; Wolf, Launhardt & Henning 2003).

Chen et al. (2012) studied the ^{12}CO(2−1) outflow in L1389 and found that CO emission is showing a bipolar morphology as seen in low-mass protostellar outflows (Arce & Sargent 2006; Jørgensen et al. 2007). The outflow position angle (measured from north increasing towards east) is estimated to be ∼125°. Chen et al. (2012) found that near the source L1389-MMS, the redshifted and blueshifted emissions show long and narrow structures (∼8500 and ∼7500 au in size, respectively). These structures are found to be extending in the east–west direction and overlapping on each other. Chen et al. (2012) gave various possibilities for this extended emission and considered that the molecular outflow is driven by L1389-MMS, as the most likely scenario. This is different from the structure of bipolar outflows from L1389-IRS.

Chen et al. (2012) studied the L1389 in submillimetre wavelength using SCUBA and mapped the dense core in 850 μm emission. Plane-of-the-sky position angle of the major axis of the core measured from 850 μm emission map is ∼135°. Hence, the minor axis position angle of the L1389 core is ∼45°. Similar to L1415, we performed the CSAR analysis on the available 250 μm *Herschel*-SPIRE image of L1389 also. We considered the head part of this cometary-shaped cloud where the *IRAS* source is detected (Chen et al. 2012) for the CSAR analysis. The ellipse is fitted to the round-shaped head part where the dense core with L1389-IRS is embedded. The lower panel of Fig. 7 shows the ellipse fitted to L1389 *Herschel* image. The minor axis position angle of the fitted ellipse is found to be ∼50° which is similar to the value found in 850 μm emission map of L1389 by Chen et al. (2012). We adopted this position angle for our further analysis of the results in L1389 core.

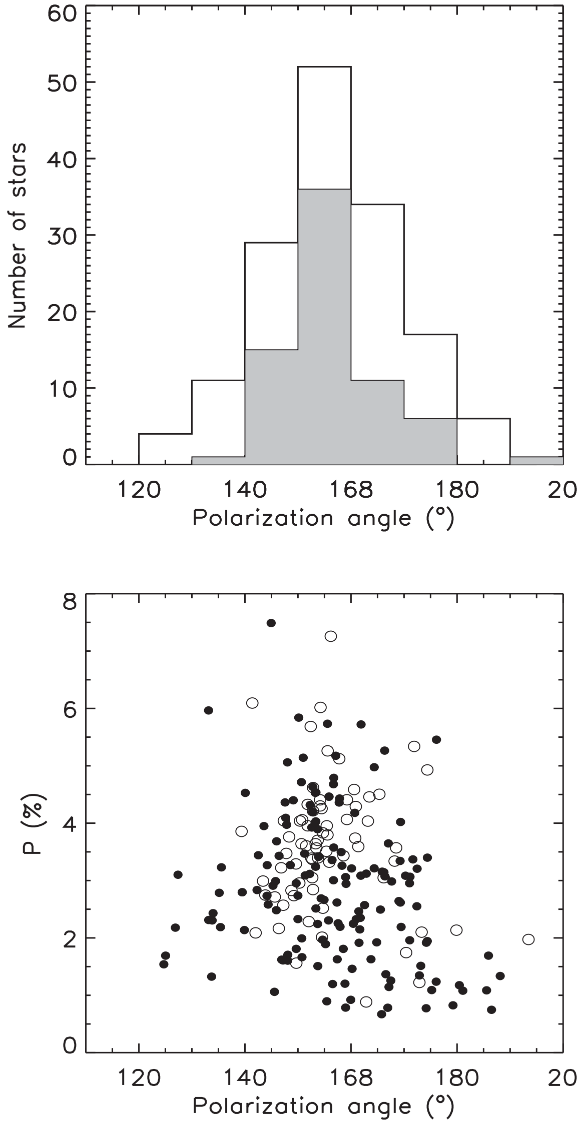

Figure 5. Histograms of θ_P (upper panel) and distribution of P with position angles (lower panel) of the stars corresponding to the two populations towards L1415 dominated by two velocity components with V_{LSR} −5.5 and −0.5 km s^{-1}. The two populations are shown using open and filled histograms in upper panel and open and filled circles in lower panel, respectively.

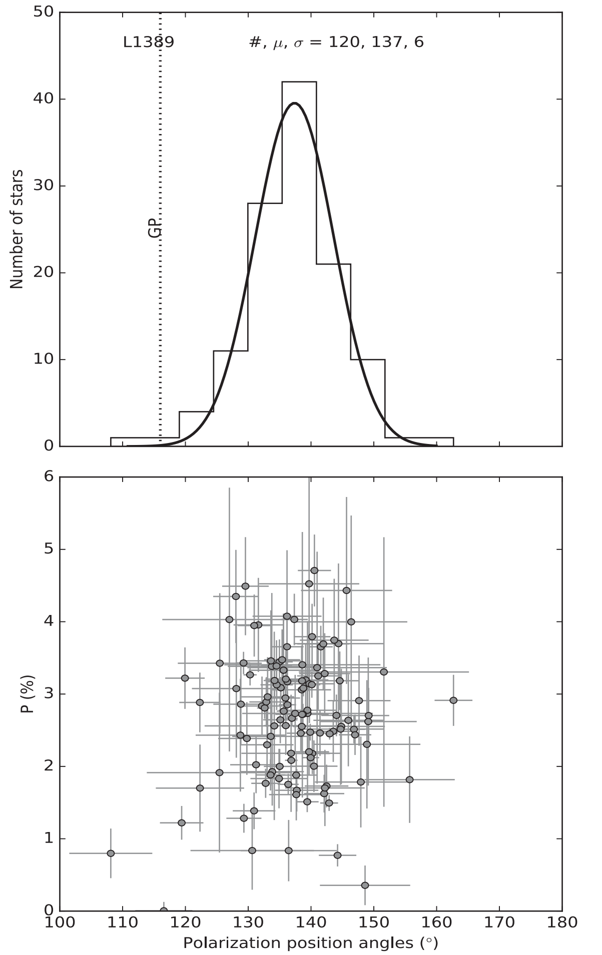

Figure 6. Upper panel: Gaussian fitted histogram of θ_P with bin size 10° in L1389. The orientation of Galactic plane at the latitude of the cloud is shown using dotted line. Lower panel: distribution of P with θ_P of the stars measured towards L1389 shown with filled circles. The submillimetre polarization measurements in L1389 using SCUBAPOL (Matthews et al. 2009) are also plotted using filled star symbols.

4 DISCUSSION

4.1 Distance of the clouds

L1415 is located in between a complex of dark clouds L1387 to L1439 which covers ∼10° at the boundaries between Camelopardalis and Auriga. Dame et al. (1987), Digel et al. (1996) and Brunt, Kerton & Pomerleau (2003) published the surveys of molecular ^{12}CO emission in Camelopardalis and the neighbouring regions. The molecular clouds in Cam OB1 layer were found with velocities −5 to −20 km s^{-1} (Digel et al. 1996). The Camelopardalis clouds are located almost at the same distance as the Taurus–Auriga star-forming region (Straižys & Laugalys 2008). The CO line survey of Dame et al. (1987) shows that along the line of sight towards L1415 there are two emission components, stronger one at V_{LSR} −5.2 km s^{-1} and weaker one at 0 km s^{-1}. In our TRAO observations of L1415 using ^{12}CO line, we detected these two components at V_{LSR} −5.5 and −0.5 km s^{-1}, respectively. Hence, L1415 can reasonably be assumed as the part of Camelopardalis complex. An upper limit of the distance of L1415 can be assumed based on to stellar population model of Robin et al. (2003). This model predicts the number of foreground stars based on to the limiting magnitude and distance dependence of the cumulative number of stars in the cloud direction finding a maximum distance of 190 pc for an average value of 0.5 foreground stars and 250 pc for 1 foreground star. The results were consistent with the study of L1415 by Snell (1981). In this work, we tried to find the distance of L1415 with the help of stars projected towards the cloud for which polarization measurements are available in the Heiles catalogue (Heiles 2000). We selected the stars from this catalogue lying within a region of 15° around L1415. Fig. 8 shows the variation of the degree of polarization and polarization position angles of these stars from Heiles catalogue (Heiles 2000) with their distances. The distance of these stars are calculated using the parallax measurements given by van Leeuwen (2007). A sudden change in the polarization values of these stars can be noticed within the distances 170 and 250 pc suggesting the distance of the cloud is somewhere in this range. We have adopted the distance of L1415 as 250 pc. The analysis supporting this distance of L1415 is explained in Section 4.2.

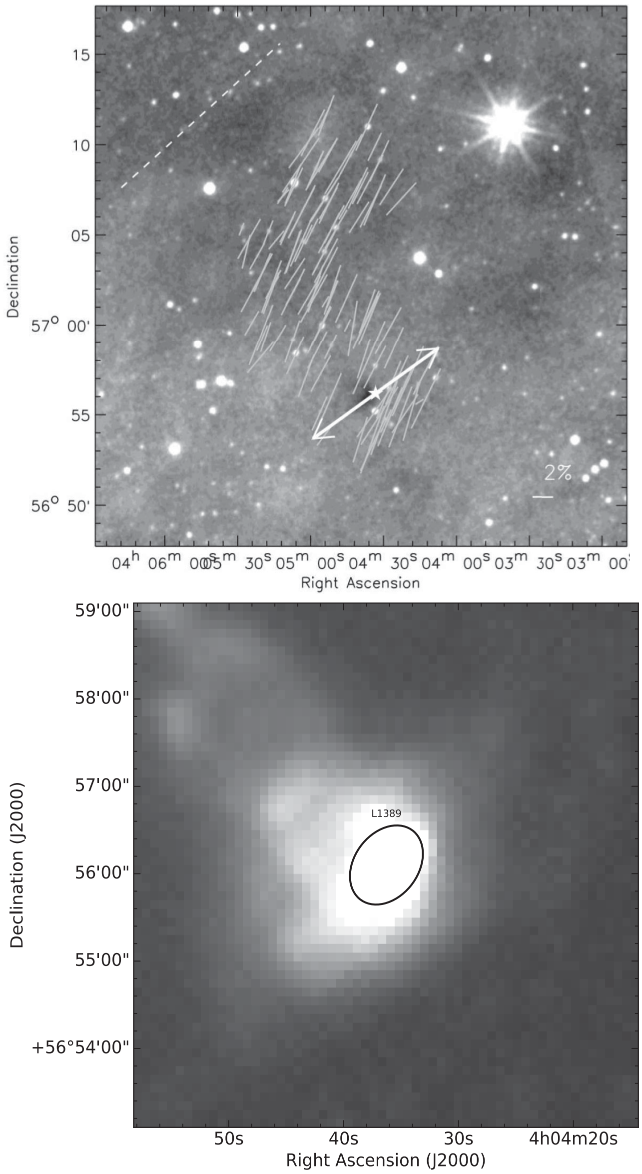

Figure 7. Upper panel: Polarization vectors of the stars observed towards L1389 plotted on 0°.5 × 0°.5 *WISE* 12 μm images after subtracting the foreground polarization contribution. The double arrow headed line shows the direction of CO outflow from L1389-IRS (shown by star symbol) and the broken line shows the orientation of the Galactic plane. The vector with 2 per cent polarization is shown as reference. Lower panel: ellipses fitted to the *Herschel* SPIRE 250 μm image of L1389 for estimating the minor axis position angle using CSAR.

The distance of L1389 is reported ranging from 210 (van Leeuwen 2007) to 300 pc (Dame et al. 1987). The distance was derived by Launhardt & Henning (1997) based on association in projected space and radial velocities with other clouds in Lindblad Ring. The Lindblad Ring structures have a mean distance of ∼300 pc (Dame et al. 1987) in the direction of L1389. A bright star HD 25347 with spectral type G5 III at a distance of 210±40 pc (van Leeuwen 2007), is located approximately 11 arcmin (0.65 pc at 200 pc) to the south of L1389 cloud. This star could be responsible for the cometary shape of the cloud and cloudshine from the rim if it is located at similar distance to that of the globule. Assuming the possible association with HD25347 and Lindblad ring, Launhardt et al. (2010) estimated a distance of 250±50 pc for L1389. We have also adopted the distance of L1389 as ∼250 pc for our further analysis.

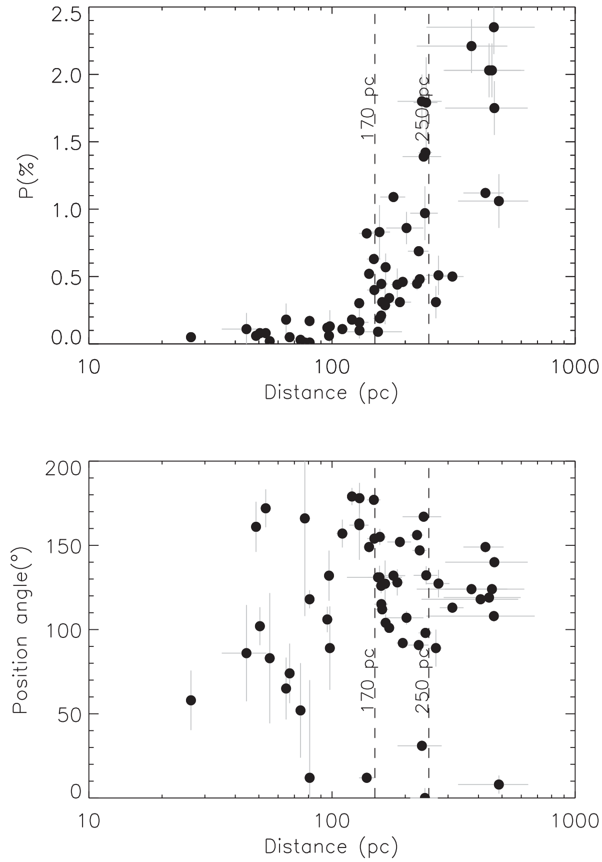

Figure 8. Variation of degree of polarization (upper panel) and position angle (lower panel) of the stars taken from Heiles catalogue (Heiles 2000) in a region of 15° around L1415, with their distances shown. The distance of these stars are measured using the parallax measurements given by van Leeuwen (2007).

4.2 Subtraction of interstellar polarization

The polarization measurements provide magnetic field morphology in the plane-of-the-sky averaged over total line of sight and weighted by the density and the alignment efficiency of the dust grains. But, in principle, to obtain the actual magnetic field morphology in a cloud, the foreground polarization contribution has to be excluded. From the previous polarization studies by us towards the clouds located at distances less than ∼500 pc (e.g. Soam et al. 2013; Neha et al. 2016) and from the literature (Li et al. 2009), it was found that the change occurred to the values of the θ_P after correcting for the foreground contribution is not noteworthy specially if the observed P is relatively higher (i.e. $\gtrsim$1 per cent). To test this fact more clearly, we subtracted the foreground contribution from L1415 (at a distance of ∼250 pc) polarization measurements in this work.

We made a search of stars that are located within a circular region of 2°.0 radius around L1415 and with their parallax measurements available from *Hipparcos* satellite (van Leeuwen 2007). We rejected the peculiar stars (emission line stars, stars in a binary or multiple system or are peculiar according to the information provided by the Simbad) and considered the normal stars for subtracting the polarization component due to the foreground material from our

Table 4. R_c-band polarization results of foreground stars towards L1415 and L1389.

Id	Star name	V (mag)	$P \pm \sigma_P$ (%)	$\theta \pm \sigma_\theta$ (°)	D^a (pc)
1	HD 30136	6.8	0.12 ± 0.09	163 ± 11	127
2	HD 30696	7.9	0.44 ± 0.06	167 ± 3	129
3	HD 30583	7.7	0.45 ± 0.05	169 ± 2	143
4	HD 30480	8.9	0.44 ± 0.07	167 ± 3	190
5	BD+54°792	9.9	1.26 ± 0.08	181 ± 1	240
6	HD 232997	9.0	0.24 ± 0.05	177 ± 4	260
7	HD 29945	8.3	0.48 ± 0.06	163 ± 3	261
8	HD 30326	8.4	1.11 ± 0.06	160 ± 1	292
9	HD 29720	8.5	0.99 ± 0.07	181 ± 1	328
10	HD 21846	8.2	0.71 ± 0.05	171 ± 1	347
11	HD 22181	7.3	0.70 ± 0.05	184 ± 2	350
	Polarization results for two foreground stars towards L1389				
1	HD 25641	6.8	0.20 ± 0.10	163 ± 11	75
2	HD 25021	8.9	0.16 ± 0.07	167 ± 3	140

Note. [a]Distances are estimated using the *Hipparcos* parallax measurements taken from van Leeuwen (2007).

observed values. 11 stars are found for which the parallax measurements are available in the catalogue produced by van Leeuwen (2007). We selected only those stars for which error in parallax and the parallax values are ≤0.5. These selected 11 stars are shown in Table 4. Similar to the target stars, these stars were also observed in R band using AIMPOL.

The polarimetric results of the foreground stars are shown in Table 4. Distribution of the degree of polarization and position angle of these stars is shown in the lower panel of Fig. 1 shown with filled star symbols. The variation of P and θ_P of these stars with their corresponding distances are given in Fig. 9. The distances to the 11 stars foreground to L1415 range from ∼127 to ∼350 pc. As expected, the degree of polarization is found to increase with the distance. There is a jump in degree of polarization at a distance of at around 240 pc. Since the distance of L1415 is assumed to be 250 pc, therefore we considered the four stars towards L1415 which are at distances less than the 240 pc for the foreground polarization subtraction from target stars. The star at 240 pc and 1.26 per cent polarization falls in the uncertainty limits of the distance of L1415 hence we did not consider this star for subtraction.

We calculated the mean value of the Stokes parameters corresponding to these stars i.e. $Q_{\rm fg}$ (=$P\cos2\theta$) and $U_{\rm fg}$ (=$P\sin2\theta$) using the observed values of the degree of polarization and the position angles. The Stokes parameters thus estimated are found to be $Q_{\rm fg} = 0.330$ and $U_{\rm fg} = -0.162$. For removing the foreground contribution of interstellar polarization from our observed values, the Stokes parameters corresponding to the target stars, $Q_\star$ and $U_\star$ were calculated. The intrinsic polarization of target stars are represented by Stokes parameters Q_i and U_i and calculated using the relations

$$Q_i = Q_\star - Q_{\rm fg}, U_i = U_\star - U_{\rm fg}. \quad (2)$$

We then estimated the intrinsic degree of polarization P_i and position angle θ_i of the target stars using the equations

$$P_i = \sqrt{(Q_i)^2 + (U_i)^2}, \theta_i = 0.5 \times \tan^{-1}\left(\frac{U_i}{Q_i}\right). \quad (3)$$

We did not notice a significance change in the polarization values after correcting for the foreground contribution. This may be because the mean value of P in foreground stars is very small (i.e. 0.63 per cent). We observed two stars foreground to L1389 (see Table 4) and followed the similar procedure for the foreground polarization subtraction from L1389. We did not notice any significant change in the polarization measurements of L1389.

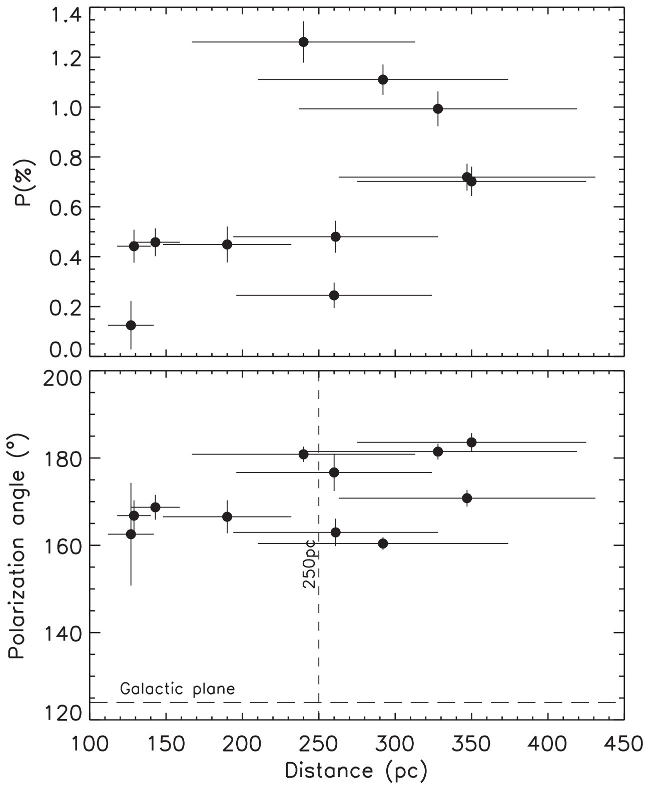

Figure 9. Variation of degree of polarization and position angle of foreground stars observed towards L1415 with their distances. The distances of these stars are estimated using the parallax measurements given by van Leeuwen (2007).

4.3 Outflow direction and magnetic fields

The angular offsets between the various quantities in five cores with Very Low Luminosity Objects (VeLLOs; Soam et al. 2015) and the two cores studied in this work are shown in Table 5. This table shows the angular offset between core scale magnetic field ($\theta_B^{\rm sub}$, obtained from the submillimetre polarization measurements), envelope magnetic field ($\theta_B^{\rm opt}$, obtained from the optical polarization measurements), outflow directions ($\theta_{\rm out}$) and minor axis ($\theta_{\rm min}$) of the cloud cores. The caution must be taken while interpreting these angular offsets as calculation are solely made between two projected quantities.

Both the clouds L1415 and L1389 have been found to be associated with collimated outflow activities from the central sources. The embedded L1415-IRS is found to be associated with HHOs (Stecklum et al. 2007). HHOs (Herbig 1950; Haro 1952) are the tracers of pre-main-sequence stars (Reipurth & Bally 2001). The presence of HHOs in the deeply embedded young stellar objects makes the association of jets evident and the radial velocity similarities of HHOs suggest that the outflow orientation is almost close to the plane-of-the-sky (Stecklum et al. 2007). The NIR morphology of L1415-IRS is indicating a bipolar outflow seen in 2.16 µm (Stecklum et al. 2007). If we join the positions of HHOs and the L1415-IRS with a line, the outflow axis in the plane-of-the-sky is found to be with position angle as ∼10° (from north increasing

Table 5. Mean magnetic field position angles and angular offsets between magnetic fields, cloud minor axis, and outflows in the core with low-luminosity objects. We have adopted some of the quantities (shown with[a]) from our previous work in Soam et al. (2015) for the purpose of increasing our sample in this study.

Cloud Id.	θ_B^{opt}	θ_B^{sub}	$\lvert\theta_B^{opt}-\theta_B^{sub}\rvert$	$\lvert\theta_B^{opt}-\theta_{min}\rvert$	$\lvert\theta_B^{sub}-\theta_{min}\rvert$	$\lvert\theta_B^{opt}-\theta_{out}\rvert$	$\lvert\theta_B^{sub}-\theta_{out}\rvert$	$\lvert\theta_{out}-\theta_{min}\rvert$	$\sigma_{\theta_B^{opt}}$
	(deg)	(°)	(°)	(°)	(°)	(°)	(°)	(°)	
(1)	(2)	(3)	(4)	(5)	(6)	(7)	(8)	(9)	(10)
IRAM 04191[a]	112	44	68	82	14	84	16	2	13
L1521F[a]	22	–	–	60	–	53	–	7	13
L328[a]	44	–	–	–	–	24	–	–	21
L673-7[a]	47	–	–	47	–	8	–	55	48
L1014[a]	15	–	–	55	–	15	–	40	13
L1415	155	–	–	50	–	35	–	15	10
L1389	137	151	14	87	101	12	26	75	06

Notes. opt: optical data; sub: submillimetre data; min: minor axis of the clouds; out: outflow direction from the VeLLO;
[a]Soam et al. (2015).

towards east). In L1389, the position angle of outflow is measured using $^{12}CO(2-1)$ molecular line observations (Chen et al. 2012). The outflow in L1389 is found to be well collimated with a plane-of-the-sky position angle of ∼125° (Chen et al. 2012). The position angle of outflows measured in the plane-of-the-sky can be uncertain by ∼10°−15° as noticed in our previous study (Soam et al. 2015).

The angular offsets between θ_B^{opt} and θ_{out} for L1415 and L1389 are 35° and 12°, respectively (column 7 of Table 5). The mean value of these offsets is 23°. The previous study of magnetic field in four cores with VeLLOs (Soam et al. 2015) reported the mean offset of 25°. The mean value of offset from previous study and this study is 24°. The outflows from protostars are thought to generate turbulence in the surrounding medium making the relatively weak magnetic fields scrambled which can further misalign the core and envelope magnetic fields. The estimated outflow parameters for low-luminosity objects suggest that these objects have outflows as highly compact, of least mass and with least energy as compared to the outflows from already known Class 0/I sources (e.g. Belloche et al. 2002; Wu et al. 2004; Bourke et al. 2006; Pineda et al. 2011). To test this scenario, we checked the distribution of outflow force and the offsets found in the cores with low-luminosity objects (see Fig. 10). The momentum flux values of these sources are adopted from literature i.e. IRAM04191 (André, Motte & Bacmann 1999), L1521F (Takahashi, Ohashi & Bourke 2013), L328 (Lee et al. 2013), L673-7 (Schwarz, Shirley & Dunham 2012), L1014 (Bourke et al. 2005) and L1389 (Chen et al. 2012). The sources with least energetic outflows are expected to have the better alignment between θ_B^{opt} and θ_{out}. However, it should be noted that the values of outflow force can be largely uncertain by many unknown parameters. For instance, Lee et al. (2013) calculated the momentum flux of L328-IRS by assuming an averaged inclination angle (i.e. $i = 57\overset{\circ}{.}3$). In Fig. 10, if we exclude the case of IRAM0419 (with a possible different environment; Soam et al. 2015), the envelope magnetic fields and the outflows are found to be aligned in L1014, L1389 and L328 cores with relatively lower outflow forces.

The dependence of alignment of the outflow, with local magnetic field at ∼10 au scale, on the magnetic field strength is tested by Matsumoto & Tomisaka (2004) based on the magnetohydrodynamic simulations. Their study suggest that in a slowly rotating, magnetized molecular cloud core undergoing gravitational collapse, the alignment is independent of the magnetic field strengths assumed in simulations. But the dependence of alignment on the magnetic field strength is considered on the cloud scale. A better alignment between outflows and magnetic field orientation is noticed in stronger magnetic fields. But such correlation is not noticed in the studies

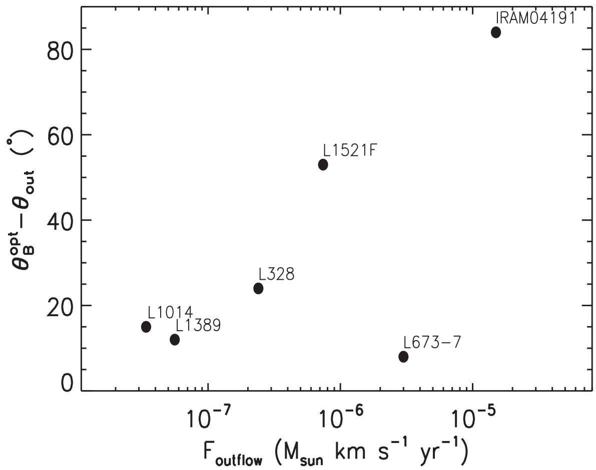

Figure 10. Variation of offset between θ_B^{opt} and θ_{out} in the cores with VeLLOs (Soam et al. 2015) and the L1389 (this work) with the outflow momentum flux. The momentum flux values of these sources are adopted from literature i.e. IRAM04191 (André et al. 1999), L1521F (Takahashi et al. 2013), L328 (Lee et al. 2013), L673-7 (Schwarz et al. 2012), L1014 (Bourke et al. 2005) and L1389 (Chen et al. 2012).

made to test the relative alignment between outflows and envelope magnetic fields such as in T-Tauri stars in the Taurus molecular cloud (Ménard & Duchêne 2004). Targon et al. (2011) used the optical polarimetric technique and found the randomly distributed offsets between magnetic fields and outflow orientations in the protostars with different ages. However, Chapman et al. (2013) noticed a statistical evidence of alignment in the study of class 0/I sources. The lack of alignment between outflows and envelope magnetic fields in relatively evolved T-Tauri stars may be present due to the injection of more turbulence from the outflows to their surrounding resulting into randomization of magnetic fields (Chapman et al. 2013). The low-luminosity sources are expected to inject the least possible turbulence into their surroundings and hence causing lowest scrambling of the magnetic fields. This may result into clouds retaining their initial field morphologies. In this work and our previous work on VeLLOs, we found an alignment in the outflows and magnetic fields.

4.4 Magnetic field strength using classical CF technique

We attempted to understand the relation between magnetic field strength and the alignment of outflows and magnetic fields towards the clouds with low-luminosity stars. We used the updated Chandrasekhar–Fermi (CF) relation ($B_{\rm pos} = 9.3\sqrt{n(H_2)}\delta v/\delta\theta$) (Chandrasekhar & Fermi 1953; Ostriker, Stone & Gammie 2001; Crutcher 2005) to estimate the plane-of-the-sky component ($B_{\rm pos}$) of the magnetic field strengths in L1415 and L1389. In this relation, $n(H_2)$ shows the number density of the molecular hydrogen which is the major constituent of the clouds, δv represents the velocity dispersion and the dispersion in $\theta_{\rm P}$ is shown using $\delta\theta$. From our TRAO observations, we checked the line width values at various positions (coinciding with our polarization observation positions) of ^{12}CO(1−0) emission in L1415 and found that these values vary only by $\Delta v = 0.05$ km s^{-1}. Hence, we measured the average ^{12}CO(1−0) line widths, $\Delta v = 1.65 \pm 0.03$ km s^{-1} and 1.64 ± 0.02 km s^{-1} corresponding to the two components in line of sight towards L1415, respectively. We estimated the column density ($N(H_2)$) from the extinction using the relation $N(H_2)/A_V = 9.4 \times 10^{20}$ cm^{-2} mag^{-1} from Bohlin, Savage & Drake (1978). The average value of extinction traced by the stars lying behind the cloud (distance ≥250 pc) observed in this study is found to be ∼0.9 mag. The angular diameter of the cloud is found to be ∼22 arcmin. Considering 250 pc as the distance to L1415, the value of $n(H_2)$ is calculated to be ∼200 cm^{-3}. We used this value of volume density to estimate the magnetic field strength in the regions up to which optical observations were made in L1415. The $\delta\theta$ used to estimate the field strength is calculated from the standard deviation in $\theta_{\rm P}$ which was obtained by Gaussian fitting to the position angles. We have corrected the dispersion in $\theta_{\rm P}$ by uncertainty in $\theta_{\rm P}$ (Lai et al. 2001; Franco, Alves & Girart 2010). We adopted the procedure explained by Franco et al. (2010) according to which the dispersion in position angles is corrected in quadrature by the polarization angle using $\Delta\theta = ({\sigma_{\rm std}}^2 - \langle\sigma_\theta\rangle^2)^{1/2}$, where the mean error $\langle\sigma_\theta\rangle$ was estimated from $\langle\sigma_\theta\rangle = \Sigma\sigma_{\theta i}/N$, where $\sigma_{\theta i}$ is the estimated uncertainty in the star's polarization angle.[2] Considering these values, we estimated a magnetic field strength in the regions of L1415 where two components of CO emission with different $V_{\rm LSR}$ are detected. The magnetic field strengths in these regions are found to be ∼30 ± 18 and ∼25 ± 11 µG, respectively. The uncertainties in the magnetic field strengths have been measured using the uncertainties in velocity dispersion and the position angles. Thus, the mean value of the magnetic field strength in L1415 is ∼28 ± 15 µG. The CO line width information for L1389 ($\Delta v = 2.0$ km s^{-1}) is adopted from Chen et al. (2012). Using the similar estimation method and using the polarization data on head part of L1389, we obtained a magnetic field strength of ∼149 µG in L1389 (uncertainty in the $B_{\rm pos}$ is not estimated here because the uncertainty in the velocity dispersion is not known). The typical uncertainty ($\sigma B_{\rm pos}$) in the field strength is found to be ∼$0.5B_{\rm pos}$ by considering the uncertainties in $\theta_{\rm P}$ and dispersion velocity. Based on to the present study and the study of magnetic field in cores with VeLLOs by Soam et al. (2015), we noticed that the alignment is better in the cores with stronger magnetic fields but our finding is not statistically significant.

4.5 Caveats of CF technique

The CF technique has been used as a convenient tool to estimate the interstellar medium magnetic field strength but the results estimated from this technique carries significant uncertainties. The basic assumption of the CF method is that it is applicable in the cases where $\delta\theta < 25°$ (Ostriker et al. 2001). This assumption is the limitation in using this classical method. Ostriker et al. (2001) and Heitsch et al. (2001) for the first time show that this technique results into overestimation of the field strength over a coarser resolution. According to recent consensus, structure function (SF) analysis is proved to be a powerful statistical tool to estimate the magnetic field intensity on finer resolutions and relation between large-scale and turbulent component of the magnetic fields in the molecular clouds (Falceta-Gonçalves, Lazarian & Kowal 2008; Hildebrand et al. 2009; Houde et al. 2009; Franco et al. 2010). This method suggests that the analysis of small-scale randomness in the magnetic field lines could estimate the magnetic field strength.

4.6 Magnetic field strength using structure function analysis

SF of the polarization maps can be used as a technique to measure the magnetic field intensity and to probe the small-scale perturbations using turbulent angular dispersion (Falceta-Gonçalves et al. 2008; Hildebrand et al. 2009). It infers the behaviour of the dispersion of the polarization angles as a function of the length-scale in molecular clouds. The net magnetic field, $B_{\rm o}(x)$ basically consists of large-scale regular magnetic fields and turbulent component, $B_{\rm t}(x)$. The SF is a second-order quantity which is a function of polarization angle and is defined as the average of the squared difference between the polarization angle measured at two positions separated by l (Falceta-Gonçalves et al. 2008) and the square root of this quantity is known as angular dispersion functions (ADF) and measured as shown in equation (4):

$$\langle\Delta(\phi)^2(l)\rangle^{1/2} = \left\{\frac{1}{N(l)}\sum_{n=i}^{N(l)}[\phi(x) - \phi(x+l)]^2\right\}^{1/2}. \quad (4)$$

The SF analysis can lead us to understand the magnetic field intensities at various scales and hence helps in understanding the small-scale turbulence. In other words SF can possibly be used as a tool to correlate the small-scale turbulent eddies to large-scale magnetic fields (Falceta-Gonçalves et al. 2008; Hildebrand et al. 2009; Franco et al. 2010; Santos-Lima, de Gouveia Dal Pino & Lazarian 2012; Neha et al. 2016). The flat profile of the SF suggests the size of the smallest turbulent cells (Falceta-Gonçalves et al. 2008).

The SF in range $\delta < l \ll d$ [where δ and d are correlation lengths which characterizes $B_{\rm t}(x)$ and $B_{\rm o}(x)$, respectively] can be estimated with expression shown in equation (5):

$$\langle\Delta(\phi)^2(l)\rangle_{\rm tot} \simeq b^2 + m^2l^2 + \sigma_M^2(l). \quad (5)$$

In equation (5), $\langle\Delta(\phi)^2(l)\rangle_{\rm tot}$ represents the total measured dispersion from the data. Here $\sigma_M^2(l)$ are the measurements uncertainties as a function of l and estimated by taking the mean of the variances on $\Delta\phi(l)$ in each bin. In the equation, quantity b^2 is the constant turbulent contribution measured by the intercept of the fit to the data after subtracting $\sigma_M^2(l)$. The quantity m^2l^2 is a smoothly increasing contribution along with length l where m represents the slope of this linear pattern. The ratio of turbulent component and large-scale magnetic fields can be estimated as

$$\frac{\langle B_{\rm t}^2\rangle^{1/2}}{B_{\rm o}} = \frac{b}{\sqrt{2-b^2}}. \quad (6)$$

For the clouds studied in the work, we estimated ADF and plotted it as a function of distance as shown in Fig. 11. The

[2] The uncertainty in the position angles is calculated by error propagation in the expression of polarization angle θ, which gives, $\sigma_\theta = 0.5 \times \sigma_{\rm P}/P$ in radians, or $\sigma_\theta = 28\overset{\circ}{.}65 \times \sigma_{\rm P}/P$ (see; Serkowski 1974) in degrees.

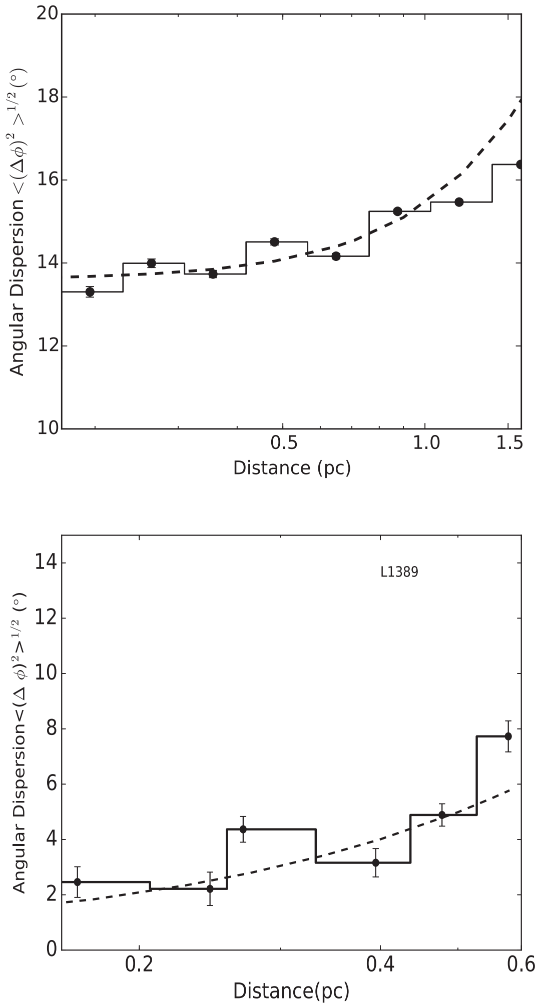

Figure 11. Distribution of ADF of the polarizations angles ($\langle\Delta(\phi)^2\rangle^{1/2}(^\circ)$) with distance for 224 stars observed towards L1415 (upper panel) and 120 stars in L1389 (lower panel). The dashed line shows the best fits to the data up to 1.5 pc in L1415 and 0.4 pc in L1389, respectively.

uncertainties though very less are also potted. In the figure, the bins represent the $\sqrt{\langle\Delta(\phi)^2(l)\rangle_{\rm tot} - \sigma_M^2(l)}$ which is ADF corrected by uncertainty. In both the clouds, we estimated net turbulent component to the angular dispersion, b and the ratio of turbulent component and the large-scale magnetic fields using equation (6). The strength of the plane-of-the-sky component of magnetic fields ($B_{\rm pos,modCF}$) is estimated from modified CF relation (Franco & Alves 2015) using equation (7). We performed the SF technique on the polarization data towards head part of L1389 because the core on the head part contains the embedded source and the velocity dispersion values are measured towards the head part only (Chen et al. 2012). The turbulent contribution to the angular dispersion, b is found to be 13°.6 ± 0°.3 (0.24 ± 0.01 rad) and 1°.9 ± 0°.4 (0.03 ± 0.007 rad) in L1415 and L1389, respectively. The values of ratio of the turbulent component and the large-scale magnetic fields estimated using equation (6) in L1415 and L1389 are found to be 0.14 ± 0.007 and 0.02 ± 0.004, respectively. The estimated values towards the two clouds studied here are shown in Table 6:

$$B_{\rm pos,modCF} = 9.3\left[\frac{2\,n_{H_2}}{\rm cm^{-3}}\right]^{1/2}\left[\frac{\Delta V}{\rm km\,s^{-1}}\right]\left[\frac{b}{1^\circ}\right]^{-1}\mu{\rm G}. \qquad (7)$$

Table 6. Parameters estimated from SF analysis.

Cloud	b (°)	$\frac{\langle B_t^2\rangle^{1/2}}{B_o}$	$B_{\rm pos,modCF}(\mu G)$
L1415	13.6	0.17	23
L1389	1.9	0.02	140

The magnetic field strengths estimated in L1415 and L1389 are found to be consistent in both CF and SF techniques. The values obtained for $B_{\rm pos,modCF}$ should be considered as the rough estimation because of the large uncertainties involved in quantities used in its measurement. Along with the uncertainties in the estimation of velocity dispersion and b, the large errors present in the estimation of the volume density may be the dominant source of uncertainties in plane-of-the-sky magnetic field strength.

4.7 Statistical view on the magnetic fields of cores with low-luminosity protostars

Among the two cores studied in this work, L1389 has inner magnetic field information inferred from submillimetre polarization observations. The inner and outer magnetic field directions have a offset of 14° implying that the field lines are anchored in high-density region and continues to low-density parts of the cloud. The angular offsets between $\theta_B{}^{\rm opt}$ and $\theta_{\rm minor}$ in L1415 and L1389 are found to be 50° and 87°, respectively. The mean value of the offsets between minor axes and magnetic fields in the two cores studied in this work and the four cores with minor axes information from Soam et al. (2015, Table 5), is found to be 63°. Thus, the minor axes and envelope magnetic fields are found to be misaligned in these cores. The magnetically dominated star formation models assume a rather aligned fields and minor axes making the above finding inconsistent to it. Basu (2000) considered the clouds as triaxial bodies and the idea of random viewing angles. This combination of assumptions can result into the average offset between magnetic fields and minor axes typically falls in the range of 10°–30°. The value of offset as ∼60° between $\theta_B{}^{\rm opt}$ and $\theta_{\rm minor}$, therefore cannot be solely explained based on projection effect.

The offset between $\theta_{\rm out}$ and $\theta_{\rm minor}$ of L1415 and L1389 are found to be 15° and 75°, respectively. The mean value of the offsets from our previous study of VeLLOs and this study becomes 32°. Four low-mass cores namely L483, L1157, L1448-IRS2 and Serp-FIR1 with Class 0 protostars were studied by Chapman et al. (2013) using 350 μm polarization observations. These observations were done to test the magnetically regulated core-collapse models. A good correlation between outflow direction and the minor axes was found in that study. Such studies allow us to use the inclination angle of the outflow as proxy of the minor axis position angle.

It has already been discussed by Soam et al. (2015) that magnetic fields are found to be preferably aligned with the Galactic plane orientation with a mean offset value of 34° in the five cores with VeLLOs. In this work also, we noticed that the magnetic fields in L1415 and L1389 are found to be parallel to the Galactic plane (with the mean offset between Galactic plane orientation and magnetic field as 27°). Thus, the mean value of the offset between Galactic plane orientation and magnetic field in the seven cores (five studied by us in Soam et al. 2015 and two in this work) is found to be 30°. Many clouds are found coupled to the Galactic plane (Klebe & Jones 1990; Kane et al. 1995), but some cases also report a decoupling between the two (Hodapp 1987; Goodman et al. 1990). The *Planck* dust polarization measurements in 353 GHz allows the precise measurements of polarization direction over all sky giving an insight into the Galactic magnetic fields (Planck Collaboration XIX 2015). The *Planck* dust polarization results in the regions studied by us show the magnetic fields aligned with the Galactic plane. Li & Henning (2011) studied six giant molecular cloud complexes in M33 and found a aligned magnetic fields with the spiral arms of M33 galaxy. This is also consistent to the results of λ 6 cm polarization survey of Galactic plane by Sun et al. (2007) who noticed a very uniform large-scale magnetic field running parallel to the Galactic plane. These studies allow us to expect a direct correlation between Galactic plane, magnetic field, minor axes and outflow direction unless the turbulence randomize the field orientation. The cloud magnetic field parallel to the galactic plane suggests that the large-scale galactic magnetic fields anchor the clouds.

5 CONCLUSIONS

We present the optical polarization study of two cores with embedded low-luminosity objects. We have drawn some combined conclusions from our study of magnetic fields in the cores with VeLLOs (Soam et al. 2015) in our previous work and low-luminosity protostars studied in this work. The main findings of this study are as follows.

(i) The angular offsets between outflow direction and envelope magnetic fields towards L1415 and L1389 are found to be 35° and 12°, respectively. The mean value of the offset in the cores with similar environments in our previous study (excluding IRAM04191) was ~25°. The sources with relatively less outflow forces are found with lesser offset between envelope magnetic field and outflow directions. This suggests that the outflows from the low-luminosity objects do not alter the inherent magnetic field morphology of the cloud and are aligned with the magnetic fields.

(ii) To estimate the plane-of-the-sky component of the magnetic field strength in the clouds, we have used the CF technique. SF technique has been used to understand the relation between large-scale magnetic fields and the turbulent component. The line width information needed for magnetic field strength estimation towards L1415 has been found using the ^{12}CO(1−0) molecular line observations from TRAO. The plane-of-the-sky component of the magnetic field strength in L1415 and L1389 using CF technique is measured to be 28±15 μG and ~149 μG, respectively, with a typical uncertainty ($\sigma B_{\rm pos}$) of ~$0.5B_{\rm pos}$. The plane-of-the-sky magnetic field strength estimated using the SF analysis was found to be 23 and 140 μG in L1415 and L1389, respectively. The magnetic field strength estimated in L1415 and L1389 are consistent in both CF and SF techniques. At the envelope scale, the dependence of alignment between the outflows and mean field direction, on the magnetic field strength is noticed in this work.

(iii) The mean value of angular offset between the envelope magnetic fields and the minor axes of L1415 and L1389 studied in this work is ~68°. The mean value of this offset in our previous study of four cores with VeLLOs was found to be ~60°. The resultant mean value of the offset in six core becomes ~65°. Thus, the minor axes of these cores are found to be misaligned with the envelope magnetic fields.

(iv) The angular offset between the outer magnetic field and inner magnetic field towards L1389 is found to be 14° suggesting the anchoring of magnetic fields from high-density core region to the low-density envelope region.

To arrive at a statistically significant conclusion, we have to map the magnetic fields in more number of cores with similar environments. Submillimetre polarization observations in future towards these sources can help us better to understand the correlation between core scale magnetic fields with the envelope fields.

ACKNOWLEDGEMENTS

Authors thank the referee for an encouraging report resulting significant improvement in the paper. The use of SIMBAD and NASA's *SkyView* facility (http://skyview.gsfc.nasa.gov) located at NASA Goddard Space Flight Center is acknowledged. AS thanks Korea Astronomy and Space Science Institute (KASI) for providing the post-doctoral research fund. CWL was supported by Basic Science Research Program though the National Research Foundation of Korea (NRF) funded by the Ministry of Education, Science, and Technology (NRF-2016R1A2B4012593). AS thanks P. Bhardwaj and V. Bhagat for their help during the optical observations. AS is thankful to the TRAO staff for their continuous support during the radio observations.

REFERENCES

Andersson B.-G., Lazarian A., Vaillancourt J. E., 2015, ARA&A, 53, 501
André P., Motte F., Bacmann A., 1999, ApJ, 513, L57
Arce H. G., Sargent A. I., 2006, ApJ, 646, 1070
Basu S., 2000, ApJ, 540, L103
Belloche A., André P., Despois D., Blinder S., 2002, A&A, 393, 927
Bohlin R. C., Savage B. D., Drake J. F., 1978, ApJ, 224, 132
Bourke T. L., Crapsi A., Myers P. C., Evans N. J., II, Wilner D. J., Huard T. L., Jørgensen J. K., Young C. H., 2005, ApJ, 633, L129
Bourke T. L. et al., 2006, ApJ, 649, L37
Brunt C. M., Kerton C. R., Pomerleau C., 2003, ApJS, 144, 47
Chandrasekhar S., Fermi E., 1953, ApJ, 118, 113
Chapman N. L. et al., 2013, ApJ, 770, 151
Chen X., Arce H. G., Dunham M. M., Zhang Q., Bourke T. L., Launhardt R., Schmalzl M., Henning T., 2012, ApJ, 751, 89
Crutcher R. M., 2004, Ap&SS, 292, 225
Crutcher R., 2005, in Chyzy K. T., Otmianowska-Mazur K., Soida M., Dettmar R.-J., eds, The Magnetized Plasma in Galaxy Evolution Magnetic Fields and Star Formation. Jagiellonian University, Krakow, p. 103
Dame T. M. et al., 1987, ApJ, 322, 706
Dennison B., 1977, ApJ, 215, 529
Dib S., Kim J., Vázquez-Semadeni E., Burkert A., Shadmehri M., 2007, ApJ, 661, 262
Dib S., Hennebelle P., Pineda J. E., Csengeri T., Bontemps S., Audit E., Goodman A. A., 2010, ApJ, 723, 425
Digel S. W., Lyder D. A., Philbrick A. J., Puche D., Thaddeus P., 1996, ApJ, 458, 561
Dolginov A. Z., Mitrofanov I. G., 1976, Ap&SS, 43, 291
Falceta-Gonçalves D., Lazarian A., Kowal G., 2008, ApJ, 679, 537
Fiedler R. A., Mouschovias T. C., 1993, ApJ, 415, 680
Franco G. A. P., Alves F. O., 2015, ApJ, 807, 5
Franco G. A. P., Alves F. O., Girart J. M., 2010, ApJ, 723, 146
Galli D., Shu F. H., 1993, ApJ, 417, 243
Goodman A. A., 1996, in Roberge W. G., Whittet D. C. B., eds, ASP Conf. Ser. Vol. 97, Polarimetry of the Interstellar Medium. Astron. Soc. Pac., San Francisco, p. 325
Goodman A. A., Bastien P., Menard F., Myers P. C., 1990, ApJ, 359, 363
Haro G., 1952, ApJ, 115, 572
Heiles C., 2000, AJ, 119, 923
Heitsch F., Zweibel E. G., Mac Low M.-M., Li P., Norman M. L., 2001, ApJ, 561, 800
Herbig G. H., 1950, ApJ, 111, 11
Hildebrand R. H., Kirby L., Dotson J. L., Houde M., Vaillancourt J. E., 2009, ApJ, 696, 567
Hoang T., Lazarian A., 2014, MNRAS, 438, 680
Hoang T., Lazarian A., Andersson B.-G., 2015, MNRAS, 448, 1178

Hodapp K.-W., 1987, ApJ, 319, 842
Houde M., Vaillancourt J. E., Hildebrand R. H., Chitsazzadeh S., Kirby L., 2009, ApJ, 706, 1504
Jørgensen J. K. et al., 2007, ApJ, 659, 479
Kandori R., Dobashi K., Uehara H., Sato F., Yanagisawa K., 2003, AJ, 126, 1888
Kane B. D., Clemens D. P., Leach R. W., Barvainis R., 1995, ApJ, 445, 269
Kirk J. M. et al., 2013, MNRAS, 432, 1424
Klebe D., Jones T. J., 1990, AJ, 99, 638
Lai S.-P., Crutcher R. M., Girart J. M., Rao R., 2001, ApJ, 561, 864
Larson R. B., 1969, MNRAS, 145, 271
Launhardt R., Henning T., 1997, A&A, 326, 329
Launhardt R. et al., 2010, ApJS, 188, 139
Launhardt R. et al., 2013, A&A, 551, A98
Lazarian A., 2003, J. Quant. Spectrosc. Radiat. Transfer, 79, 881
Lazarian A., 2007, J. Quant. Spectrosc. Radiat. Transfer, 106, 225
Lee C. W., Kim M.-R., Kim G., Saito M., Myers P. C., Kurono Y., 2013, ApJ, 777, 50
Levy E. H., Lunine J. I., 1993, J. Br. Astron. Assoc., 103, 266
Li H.-B., Henning T., 2011, Nature, 479, 499
Li H.-b., Dowell C. D., Goodman A., Hildebrand R., Novak G., 2009, ApJ, 704, 891
Lindblad P. O., Grape K., Sandqvist A., Schober J., 1973, A&A, 24, 309
Mac Low M.-M., Klessen R. S., 2004, Rev. Mod. Phys., 76, 125
Masunaga H., Miyama S. M., Inutsuka S.-i., 1998, ApJ, 495, 346
Matsumoto T., Tomisaka K., 2004, ApJ, 616, 266
Matthews B. C., McPhee C. A., Fissel L. M., Curran R. L., 2009, ApJS, 182, 143
Ménard F., Duchêne G., 2004, A&A, 425, 973
Mouschovias T. C., 1991, ApJ, 373, 169
Neha S., Maheswar G., Soam A., Lee C. W., Tej A., 2016, A&A, 588, A45
Olofsson S., Olofsson G., 2010, A&A, 522, A84
Ostriker E. C., Stone J. M., Gammie C. F., 2001, ApJ, 546, 980
Pineda J. E. et al., 2011, ApJ, 743, 201
Planck Collaboration XIX, 2015, A&A, 576, A104
Raga A. C., Canto J., 1996, MNRAS, 280, 567
Ramaprakash A. N., Gupta R., Sen A. K., Tandon S. N., 1998, A&AS, 128, 369
Rautela B. S., Joshi G. C., Pandey J. C., 2004, Bull. Astron. Soc. India, 32, 159
Reipurth B. ed. 1999, A General Catalogue of Herbig-Haro Objects, 2nd Edition. Available at: http://casa.colorado.edu/hhcat
Reipurth B., Bally J., 2001, ARA&A, 39, 403
Robin A. C., Reylé C., Derrière S., Picaud S., 2003, A&A, 409, 523
Santos-Lima R., de Gouveia Dal Pino E. M., Lazarian A., 2012, ApJ, 747, 21
Schmidt G. D., Elston R., Lupie O. L., 1992, AJ, 104, 1563
Schwarz K. R., Shirley Y. L., Dunham M. M., 2012, AJ, 144, 115
Serkowski K., 1974, in Carleton N., ed., Methods of Experimental Physics. Academic Press, New York, p. 361
Shu F. H., Adams F. C., Lizano S., 1987, ARA&A, 25, 23
Snell R. L., 1981, ApJS, 45, 121
Soam A., Maheswar G., Bhatt H. C., Lee C. W., Ramaprakash A. N., 2013, MNRAS, 432, 1502
Soam A., Maheswar G., Lee C. W., Dib S., Bhatt H. C., Tamura M., Kim G., 2015, A&A, 573, A34
Stecklum B., Melnikov S. Y., Meusinger H., 2007, A&A, 463, 621
Straiżys V., Laugalys V., 2008, in Reipurth B., ed., Handbook of Star Forming Regions, Vol. I. The Northern Sky. Astron. Soc. Pac., San Francisco, p. 294
Sun X. H., Han J. L., Reich W., Reich P., Shi W. B., Wielebinski R., Fürst E., 2007, A&A, 463, 993
Takahashi S., Ohashi N., Bourke T. L., 2013, ApJ, 774, 20
Targon C. G., Rodrigues C. V., Cerqueira A. H., Hickel G. R., 2011, ApJ, 743, 54
van Leeuwen F., 2007, A&A, 474, 653
Ward-Thompson D., Scott P. F., Hills R. E., Andre P., 1994, MNRAS, 268, 276
Whittet D. C. B., 2005, in Adamson A., Aspin C., Davis C., Fujiyoshi T., eds, ASP Conf. Ser. Vol. 343, Astronomical Polarimetry: Current Status and Future Directions. Astron. Soc. Pac., San Francisco, p. 321
Wilking B. A., Lebofsky M. J., Kemp J. C., Martin P. G., Rieke G. H., 1980, ApJ, 235, 905
Wolf S., Launhardt R., Henning T., 2003, ApJ, 592, 233
Wu Y., Wei Y., Zhao M., Shi Y., Yu W., Qin S., Huang M., 2004, A&A, 426, 503

This paper has been typeset from a TEX/LATEX file prepared by the author.